Dynamic earthquake source inversion with Generative Adversarial Network priors

Jan Premus[1], Jean Paul Ampuero[1]

[1] Université Côte d'Azur, IRD, CNRS, Observatoire de la Côte d'Azur, Geoazur, Nice, France

Corresponding author: Jan Premus (janpremus@seznam.cz)

This is a non-peer-reviewed preprint submitted to EarthArXiv, the manuscript has been also submitted to *Journal of Geophysical Research: Solid Earth.*

Key Points:

- We develop a 2-stage Bayesian dynamic source inversion using Wasserstein Generative Adversarial Network to approximate the posterior of stage 1 as a prior for stage 2.
- We conduct a thorough synthetic test, estimating statistical properties of the original dynamic inversion and our 2-stage approach, demonstrating better performance of the latter.
- We discuss the correlations between dynamic parameters that occurred as a result of inversions.

Abstract

Dynamic source inversion of earthquakes consists of inferring frictional parameters and initial stress on a fault consistent with recorded seismological and geodetic data and with dynamic earthquake rupture models. In a Bayesian inversion approach, the nonlinear relationship between model parameters and data requires a computationally demanding Monte Carlo (MC) approach. As the computational cost of the MC method grows exponentially with the number of parameters, dynamic inversion of large earthquakes, involving hundreds to thousands parameters, is hindered by slow convergence and sampling issues. We introduce a novel multi-stage approach for dynamic source inversion. We divide the earthquake source into a hierarchical set of temporal and spatial stages. As each stage involves only a limited number of independent model parameters, their inversion converges faster. Stages are interdependent: the inversion results of an earlier stage are a prior for the next stage inversion. We use Wasserstein Generative Adversarial Networks to transfer the prior information between inversion stages. As proof-of-concept, we apply a two-stage version of our dynamic source inversion approach to a simulated earthquake scenario generated by dynamic rupture modeling. Compared to direct MC inversion, the two-stage approach achieves substantial improvements in relevant performance metrics, including integrated autocorrelation time, and a large increase in stability across several independent runs. Further application of the two-stage Bayesian inversion method will allow for expanded dynamic modeling studies of large earthquakes, paving the way towards a better understanding of earthquake physics.

Plain Language Summary

Dynamic earthquake source inversion is a systematic approach to infer earthquake physics parameters from geophysical data. However, being a nonlinear high-dimensional inverse problem, its application to large earthquakes is hindered by high computational cost exceeding the capacity of current supercomputers. In this study, we introduce a novel approach to enable dynamic source inversion of large earthquakes. We combine three innovations: a hierarchical multi-stage approach, a 2.5D approximation of the dynamic rupture problem, and a Deep Learning method based on Wasserstein Generative Adversarial Networks (GAN). Compared to direct Monte Carlo inversion, the two-stage approach achieves substantial improvements in relevant performance metrics, including integrated autocorrelation time, and a large increase in stability across several independent runs

1 Introduction

While the basic physical model of large shallow earthquakes is well established (sudden slip on a pre-existing fault caused by accumulated tectonic stress exceeding the fault strength, e.g. Kanamori and Brodsky, 2001), building a detailed physical model and explaining why a specific earthquake happens is still a major challenge. Difficulties include the complex behavior arising from the strong nonlinearity of dynamic rupture models and our limited access to observations of processes occurring at seismogenic depth. Seismic and geodetic networks, while growing in density, still offer sparse coverage in the vicinity of active faults. Even if sensor networks were extremely dense, their coverage would still be limited to Earth's surface. Additionally, the fault geometry, the mechanical properties of surrounding rocks, or the appropriate form of the constitutive law relating fault stress and slip are all subjects to uncertainty and difficult to model with high precision.

Earthquake source inversion is an inverse problem that consists of inferring parameters of the seismic source from measured geophysical data. It mathematically formalizes the construction of a physical model explaining the evolution of the earthquake. There are two main classes of finite-fault source inversion. In *kinematic* source inversion, the source model is parameterized by the space-time distribution of slip rate. In *dynamic* source inversion, it is parametrized by fault friction properties and initial stresses (the inputs of a dynamic rupture model). Due to the mentioned uncertainties, even the linear version of kinematic source inversion suffers from ill-posedness or non-uniqueness, leading to significant differences between results obtained by different inversion methods (Gallovic and Ampuero, 2015). Non-uniqueness is also prominent in dynamic source inversion: Guatteri and Spudich (2000) showed that two models with widely different values of friction properties can generate seismograms that are very similar in a given frequency band. Moreover, the non-linearity of the relationship between dynamic parameters, kinematic parameters (such as slip) and data (such as seismograms) also makes the problem ill-conditioned. On the positive side, the physics underlying dynamic rupture models acts as an additional constraint on the range of possible slip distributions, and the synthetic data produced by the dynamic forward model can be very sensitive to small changes in the dynamic parameters.

For such a non-unique inverse problem, a Bayesian formulation is more fitting, because it embraces the probabilistic nature of the problem and seeks a range of probable models instead of a single optimal one. The Bayesian inverse problem can be framed as the process of updating the knowledge available before the earthquake, represented by a prior probability density function (PDF), to a post-earthquake state of knowledge, represented by a posterior PDF, constrained by recorded data.

A common approach to solve nonlinear Bayesian inverse problems uses a Markov chain Monte Carlo (MCMC) algorithm to sample the posterior PDF. MCMC generates a stochastic sequence of discrete samples, where the next sample in the chain is chosen as a random perturbation of the previous one (Sokal, 1996; Sambridge, 2014). While the method and its successive improvements (e.g. parallel tempering) were developed to deal with multi-dimensional PDFs with non-Gaussian shapes, they still suffer from the curse of dimensionality: with increasing number of model parameters, the convergence towards models with high posterior PDF becomes exponentially more difficult.

Dynamic earthquake source inversions reach the limits of current computational capacity as they combine a large number of inverted parameters and high computational demands of the forward model, thus limiting the maximum feasible number of MCMC steps. Peyrat and Olsen (2004), Corish et al. (2007) and Ruiz and Madariaga (2013) used the neighborhood (non-MCMC) algorithm to explore the parameter space of a simplified dynamic model, assuming an elliptical rupture. Gallovic et al. (2020) performed a fully Bayesian dynamic inversion, applying a Parallel Tempering MCMC. Premus et al. (2023) and Schliwa et al. (2024) expanded the method to include rate-and-state friction and a quasi-dynamic model of postseismic slip. These inversions required hundreds of thousands to millions of dynamic model computations calculated over a wall-clock compute time period of several months.

As the popularity of Bayesian inversions increases and it is applied to problems with increasing mathematical complexity, both in terms of nonlinearity and dimensionality, and larger datasets, the MCMC approaches are being adapted and improved to better fit the scientific problems and computational resources. More efficient and scalable Hamiltonian MCMC (Betancourt, 2017; Fichtner et al., 2019) can be applied if the gradient of the likelihood function with respect to the model parameters can be evaluated or estimated efficiently. While efficient estimation of the model gradient is difficult, the adjoint model (and thus gradient) to a fully dynamic earthquake model is now available (Stiernström et al., 2024), which makes future application of the gradient-based methods possible. For the case of the kinematic source inversion, improvements of the random sampling using a Normalizing Flows machine learning algorithm (Scheiter et al., 2024), or accounting for modeling error by a cross-fade sampling method (Minson, 2024) have been applied, but not in dynamic source inversion yet. Besides MCMC approaches, physics-informed neural networks (PINNS) was recently tested for the inversion of rate-and-state friction parameters (Rucker and Erickson, 2024).

Here, we present a multi-stage approach to efficiently constrain the prior PDF of the Bayesian dynamic source inversion, thus limiting the parameter space that needs to be explored and improving the performance of the inversion. We draw our inspiration from multi-stage approaches applied to kinematic inversions (Uchide and Ide, 2007; Uchide et al., 2009; Uchide, 2013) and seismic tomography (Stuart et al., 2019). The multi-scale slip inversion (Uchide and Ide, 2007) simultaneously explores the whole earthquake rupture and in more detail (with finer resolution and higher frequencies) its initial stage from the beginning phases of the seismograms. The two-stage approach in seismic tomography (Stuart et al., 2019) takes advantage of computationally cheaper simulations to filter the proposed models and quickly reject unfeasible ones. In addition, to facilitate the sampling of the constrained prior, we reformulate it using a deep learning algorithm, Generative Adversarial Networks (GANs). The generator learns to approximate the PDF based on samples from the first-stage inversion and proposes the parameter combinations in the second-stage dynamic inversion.

The rest of this paper presents the theoretical background of Bayesian inversions and Generative Adversarial Networks in Section 2 - Theory, and introduces the 2-stage dynamic inversion method in Section 3 - Method. In Section 4, we present a synthetic test to directly compare our 2-stage method against a traditional dynamic source inversion approach. We invert for parameters of a known target dynamic earthquake model, evaluating the performance of the method in accurately and efficiently sampling the posterior PDFs. As we provide results of 5 independent MCMC runs, our results in Section 4 are also interesting to more generally gauge the accuracy and repeatability of the Bayesian inversion results.

2 Theory

2.1 Bayesian inversion and Markov Chain Monte Carlo

A dynamic earthquake source model consists of a physics-based dynamic rupture simulation that numerically solves the partial differential equations describing the propagation of seismic waves coupled to boundary conditions describing fault friction and assuming initial conditions leading to spontaneous earthquake rupture (e.g., Andrews, 1976). The dynamic model parameters m to be determined are spatially discretized versions of the on-fault distributions of initial stresses and frictional properties. For instance, one subset of model parameters can be the values of the frictional slip-weakening distance D_c evaluated at the midpoint of 2 km x 2 km cells on a grid covering the potential rupture area on the fault. The dynamic model constitutes the forward problem F providing a mapping between the model parameters and data:

$$F(m)=d+\epsilon,$$

where ϵ is the modeling error, and data d are measured seismograms and geodetic displacements. Solving the inverse problem amounts to estimating the model parameters m from the data d. We formulate the problem in the framework of Bayesian inference as an update of the knowledge about potential values of m, described as a probability density function (PDF). The prior PDF $p(m)$ represents the initial state of knowledge before accounting for the new data d. The posterior PDF $p(m \vee d)$ accounts for new data, and is estimated by following Bayes' rule:

$$p(m \vee d)=k^{-1}p(d \vee m)p(m),$$

where k is a normalization constant and $p(d \vee m)$ is the likelihood function - a statistical model of the difference between observed data and modeled data $d_m=F(m)$ produced by a forward model with given parameters m.

The shape of the likelihood function depends in principle on the shape of the measurement noise in the data and on the modeling error. The measurement noise can be assumed to have a Gaussian shape for both the GPS data and seismograms on a limited frequency spectrum. The modeling error is more dominant and harder to evaluate. While some approximations have been proposed (Duputel et al, 2015; Hallo and Gallovic, 2016), we follow Sambridge (2014) and Gallovic et al. (2020) and assume Gaussian noise with a covariance matrix C_d. The resulting likelihood function is

$$p(d \vee m) = \frac{1}{2\pi \sqrt[N]{C_d}} \exp\left[(d-d_m)^T C_d^{-1} (d-d_m)\right].$$

We further simplify it by assuming uncorrelated noise with a diagonal matrix $C_d = \sigma^2 I$ with uniform standard deviation σ:

$$p(d \vee m) = \frac{1}{2\pi\sigma^2} \exp\left[(d-d_m)^T (d-d_m)/\sigma^2\right].$$

Note that, because σ is intended to include the modeling error, it is significantly larger than the standard deviation of measurement noise.

We apply the Markov chain Monte Carlo algorithm (MCMC) to draw samples from a posterior PDF by a random walk process (Robert and Cassela, 1999; Liu, 2001). The output of the algorithm is a Markov chain: a series of draws of model parameters m_n where the $(n+1)$-th draw depends only on the n-th draw. The classical Metropolis-Hastings algorithm (Metropolis et al., 1953) generates a Markov chain using a proposal probability density function for new steps and a method for rejecting some of the proposed moves based on their likelihood. After choosing an initial chain member m_1, the following algorithm is applied recursively:

- Propose a candidate m'_{n+1} by randomly varying m_n (see Methods section 3.2 for details).
- Calculate the acceptance ratio $\alpha(m_n, m'_{n+1}) = p(d \vee m'_{n+1}) / p(d \vee m_n)$
- Draw a uniform random number $r \subset [0,1]$
    - If $r < \alpha(m_n, m'_{n+1})$ accept the candidate $m_{n+1} = m'_{n+1}$
    - If $r > \alpha(m_n, m'_{n+1})$ reject the candidate

Dynamic inversion is a nonlinear, high-dimensional problem, whose likelihood function can have a complicated shape with multiple local minima. For such an inverse problem, the Metropolis-Hastings algorithm might not efficiently sample the model parameter space (Sambridge, 2014). We thus adopt an improved parallel tempering (PT) MCMC algorithm (Geyer, 1999; Falconi and Deem, 1999). It uses several Markov chains. The i-th chain samples the “tempered” posterior distribution

$$p_i(m \vee d) = k^{-1} p^{1/T_i}(d \vee m)\, p(m).$$

The exponent $T_i \subset (1, T_{max})$ is analogous to the temperature of the *i*-th chain. Only one of the chains, the one with $T_i = 1$, samples the true posterior PDF. The samples from this chain are considered the solution of the inverse problem. Chains at higher temperatures sample tempered, smoother PDFs, and thus can explore the model parameter space faster owing to a higher acceptance rate, passing the local minima the untempered chain might get stuck in.

The information between chains is transferred by periodically proposing the exchange of models between two chains. We follow the PT algorithm of Sambridge (2014) in proposing exchanges between two randomly selected chains *i* and *j* and accepting them with the following probability:

$$\alpha_{swap}(i,j) = min¿,$$

where T and ϕ are the respective temperatures and likelihood functions. These exchanges allow the better-fitting models to move toward the main untempered chain ($T_i = 1$).

The successive samples in the Markov chain are a product of a random walk, in which sample *n+1* is obtained by randomly varying sample *n*, and thus are not fully independent draws from the posterior PDF. This manifests as a correlation between samples that decreases with the number of steps (lag) between them. The efficiency of the MCMC algorithm depends on how many steps are needed before arriving at samples that are not correlated with the starting sample (correlation coefficient close to zero). In fact, the goal is to generate a sufficiently large number of uncorrelated samples of the posterior PDF. Because the length of the Markov chain is finite and constrained by the computational demands of solving the forward model, it is of high importance to quantify the degree of correlation between samples.

The variance V of the mean $M(m)$ (Sokal, 1996) of model parameter *m* is proportional to the autocorrelations (see derivation in Supplement 1)*:*

$$V[M(m)] = \frac{\sigma^2(m)}{N} \sum_{i=-\infty}^{\infty} C^i(m,m),$$

where $\sigma(m)$ is the standard deviation of m, N is the number of steps in the chain, and $C^l(m,m)$ are the autocorrelation coefficients of the chain of the model parameter *m* at lag *l*. This is the variance of results from independent MCMC inversions of chain length N.

Expecting $C^l(m,m)$ decays rapidly with increasing lag *l*, we calculate the *integrated autocorrelation time* (IAT):

$$\tau_{\int ¿(m) = \frac{1}{2} \sum_{l=-\infty}^{\infty} \rho^l(m,m) ¿},$$

where $\rho^l(m,m) = C^l(m,m) / C^0(m,m)$. The value $2 \times \tau_{\int ¿(m)¿}$ provides an estimate of how many more random walk steps are needed to achieve the same variance as uncorrelated random draws from the posterior.

2.2 GAN priors

Bayesian MCMC inversions require to formulate the prior PDF $p(m)$ as an explicit function of model parameters m. The choices of the prior functions are usually limited to uniform or Gaussian functions (including correlation matrices) or hierarchical priors (Natesan et al., 2016; Gao and Chen, 2005). So far, only wide uniform PDFs have been used as prior in dynamic source inversions (e.g., Gallovic, 2019), including several constraints in the form of conditional statements to e.g. limit the stress drop in the nucleation zone. Such prior is much wider than the posterior PDF and represents effectively zero prior knowledge about dynamic parameters.

Recent advances in the field of machine learning have opened the way for new approaches to represent the prior PDF. In particular, Generative Adversarial Networks (GAN), a class of unsupervised machine learning algorithms (Goodfellow et al., 2014), aims at generating data that mimic a target distribution, and has been leveraged to represent the prior (Arridge et al., 2019; Holden et al., 2022; Patel et al., 2022 ; Marschall et al., 2023).

Once we train the generator on samples from the target distribution, it can generate samples mimicking the target distribution, given an input from a low-dimensional latent space. The inversion is then reformulated to seek the values of the generator inputs in the latent space. This decreases the dimensionality of the inverse problem, and the volume of the parameter space that needs to be searched by the random walk.

The GAN algorithm is based on a zero-sum game between two neural networks, a generator G and a critic C (also called discriminator). During the training process we alternately optimize the network weights of the generator $\omega^G \in R^{N_{\omega^G}}$ and of the critic $\omega^C \in R^{N_{\omega^C}}$ to minimize/maximize their cost functions.

The generator $G(\gamma, \omega^G)$ takes as input randomly chosen vectors from a multi-dimensional real latent space $\gamma \in \Omega_{latent} \subset R^{N_\gamma}$ taken from a distribution $p_{latent}(\gamma)$. It outputs samples θ from the space ($\Omega_{target} \subset R^{N_\theta}$) of the target distribution p_{target}. In the original GAN setting, the critic $C(\theta, \omega^C)$ inputs a sample $\theta \in \Omega_{target} \subset R^{N_\theta}$ and aims to discriminate between the synthetic samples from the generator (outputs 0) and real samples from the training dataset (outputs 1). During the training process, we repeatedly train the critic to correctly label the synthetic and training samples, by maximizing

$$V_C(C,G) = E_{\theta \sim p_{data}(\theta)}[\log(C(\theta, \omega^C))] + E_{\gamma \sim p_{latent}(\gamma)}[\log(1 - C(G(\gamma, \omega^G), \omega^C))],$$

where the first term is the expectation of the critic over the set of samples from the target distribution and the second term is the critic's expectation over the set of the synthetic (fake) samples.

The training of the generator aims to minimize the cost function

$$V_G(C,G)=E_{\gamma\sim p_{latent}(\gamma)}[\log(1-C(G(\gamma,\omega^G),\omega^C))],$$

which is the second term from the critic's cost function, therefore to maximize the number of generated samples classified as true samples by the critic.

The GAN training process is notoriously difficult (de Souza et al., 2023, Saxena and Cao, 2022). An equilibrium between generator and critic might not be achieved due to the interdependency of their cost functions creating an unstable system (Salimans et al., 2016). Additionally, in many setups the critic might train faster than the generator, leading to vanishing gradients - if the critic rejects all generated samples, the gradient of the cost function can become zero, providing no feedback to improve for the generator (Saxena and Cao, 2022). Mode collapse (Saxena and Cao, 2022, Salimans et al., 2016) then describes a situation where the generator generates accurate samples but with low diversity, which do not cover the whole training set.

There is a large number of promising works that seek to alleviate the training problems (see Salimans et al., 2016, Kurach et al., 2019, Gui et al., 2023 for reviews). One of the improvements is called Wasserstein GAN (WGAN) (Arjovsky et al., 2017), where the critic seeks to return the Wasserstein (or earth-mover) distance (Kantorovich, 1939) between the evaluated set of samples and the training dataset. The advantage of this formulation is that it bypasses the vanishing gradients problem - even when the generator creates samples far away from the distribution, the critics output provides a usable feedback - distance from the training dataset instead of only negative labels. The authors of the WGAN algorithm (Arjovsky et al., 2017) also report no occurrence of mode collapse in their tests.

The evaluation of the Wasserstein distance $W(\nu_1,\nu_2)$ between distributions ν_1 and ν_2 is performed using the Kantorovich-Rubinstein duality (KRD, Villani, 2008):

$$W(\nu_1,\nu_2)=sup_f[E_{\theta_1\quad\nu_1(\theta_1)}(f(\theta_1))-E_{\theta_2\quad\nu_2(\theta_2)}(f(\theta_2))],$$

where we seek a supremum over a space of 1-Lipschitz continuous (with finite gradients) functions f. We set p_{target} as θ_1 and the distribution of generators outputs $G(\gamma,\omega^G)$ for $\gamma \quad p_{latent}$ as ν_2. We seek a critic that returns the function f. Its goal is to maximize the following cost function :

$$V_{C(WGAN)}(C,G)=E_{\theta\sim p_{target}(\theta)}[C(\theta,\omega^C)]-E_{\gamma\sim p_{latent}(\gamma)}[C(G(\gamma,\omega^G),\omega^C)].$$

The generator's goal is to minimize the same cost function.

The finiteness of the gradients, originally enforced by clipping the weights of the critic (Arjovsky et al., 2017), is achieved in the WGAN-GP algorithm (Gulrajani et al., 2017) by introducing a penalty on the critics gradient into its cost function:

$$V_{C(WGAN)}(C,G)=E_{\theta\sim p_{data}(\theta)}[C(\theta,\omega^{C})]-E_{\gamma\sim p_{latent}(\gamma)}[C(G(\gamma,\omega^{G}),\omega^{C})]+\lambda E_{\gamma\sim p_{latent}(\gamma)}[(\lor ¿ \nabla_{G(\gamma)} C(G(\gamma,\omega^{G}),\omega^{C})\lor$$

.(Eq.10)

We include a sample of pseudocode, based on Gulrajani et al. (2017), and a schematic of the WGAN process in Figure 1 to better demonstrate the WGAN learning process.

Set initial weights $\omega^{C}{}_{0\square}$, $\omega^{G}{}_{0}$

for $i=1,2,\ldots,N_{steps}$ **do**

    for $j=1,2,\ldots,N_{critic}$ **do**

        for $k=1,2,\ldots,N_{batch}$ **do** *#Construct the critic cost function*

            Pick random sample of $\theta_k \in p_{target}$, $\gamma_k \in p_{latent}$

            Pick random number $\epsilon_k \in [0,1]$

            $\underline{\theta_k}=G(\gamma_k,\omega^{G}{}_{i-1})$

            $\widehat{\theta}_k=\epsilon_k\theta_k+(1-\epsilon_k)\underline{\theta_k}$

            $V^{C}{}_{k}(\omega)=C(\underline{\theta_k},\omega)-C(\theta_k,\omega)+\lambda(\lor ¿ \nabla_{\hat{\theta}} C(\hat{\theta}_k,\omega)\lor ¿_2-1)^2$

        end for

        $\omega^{C}{}_{i,j}=optimize\left(\nabla_{\omega}\frac{1}{N_{batch}}\sum_{\square}^{\square}\square V^{C}{}_{k}(\omega),\omega\right)$

    end for

    Sample a batch of N_{batch} latent variables $\gamma_k \in P_{latent}$

    $\omega^{G}{}_{i}=optimize\left(\nabla_{\omega}\frac{1}{N_{batch}}\sum_{\square}^{\square}\square -C(G(\gamma_k),\omega^{C}{}_{i,N_{batch}}),\ldots\right)$

end for

The gradient penalty coefficient λ was set to a value of 10 (as in Gulrajani et al., 2017). Additional meta parameters of the algorithm comprise the number of critic iterations per generator iteration N_{critic}, the batch size N_{batch}, total number of steps N_{step} and metaparameters of the chosen optimizer.

In every step of the algorithm we repeat N_{critic} times the optimization of the critic's weights to maximize the cost function (Eq.10) using randomly selected batches of the samples of the target distribution and the generated samples. This is followed by optimization of the generator's weights to maximize the cost function on a randomly selected batch of latent variables. We iterate these steps N_{step} times but cut off the training process if we observe a convergence, to preclude overtraining.

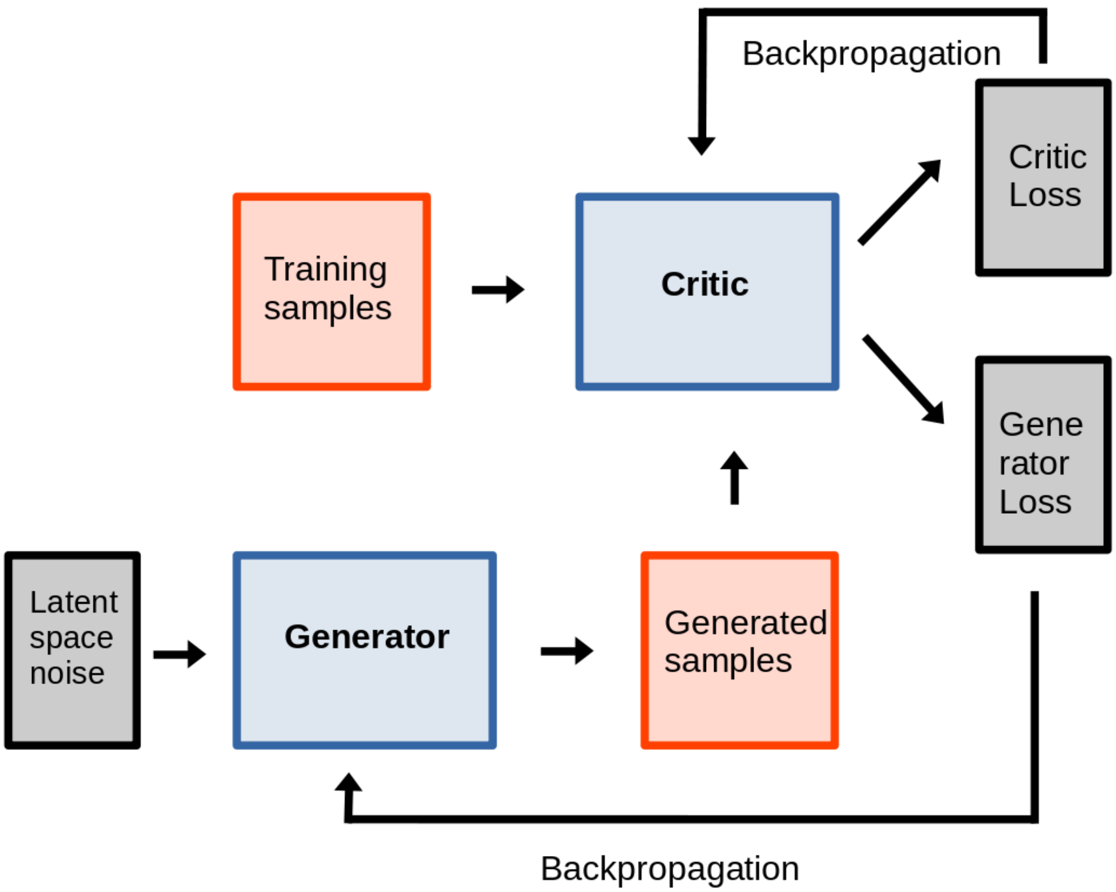

Figure 1: Scheme of GAN training process: Steps of the WGAN training process simultaneously training both the generator and the critic networks. The generator has input in the form of noise from its latent space and at every step creates a set of synthetic samples. The critic assigns a score to both generated and real training samples. The accuracy of the critic acts as a loss function for the critic training, while the score of the generated samples acts as a loss function for the generator training.

3 Method

3.1 Forward Model

MCMC inversions require large numbers of forward model computations that mostly need to be performed serially. Published dynamic source inversions typically have around thousand model parameters and require hundreds of thousands to millions of forward smulations (Gallovic et al., 2019, Schliwa et al., 2024), or tens of thousands for problems with ten parameters (Otarola et al., 2021). To obtain a sufficient number of samples of the posterior PDF, it is critical to keep low the computational demands of the forward model solver. This places a constraint on the complexity of the assumed dynamic model, as the computational cost of dynamic rupture codes quickly grows with increasing complexity of the model physics and spatio-temporal resolution. Finite difference or boundary integral methods can take between tens of seconds to minutes to model a large earthquake in a simple fault geometry, while complex geometries (e.g. Jia et al., 2023) or additional physics (such as fault plasticity (Gabriel et al., 2013)) require at least several hours of highly parallelized calculations. The goal of our dynamic source inversion approach is to model very large earthquakes, like the 2023 Turkey earthquake. We consider a simple 2.5-dimensional model to capture the basic properties of the earthquake physics while keeping the computational demands of the forward model and the dimension of the problem to a necessary minimum. We employ a spectral element (Kaneko et al., 2008; Galvez et al., 2014) dynamic rupture code in 2D (Sem2dpack, Ampuero et al., 2024) to model the rupture propagation. Following Weng and Ampuero (2019), we efficiently handle large ruptures with high aspect ratio (much longer than wide) by adopting a 2.5D approximation that solves for source properties averaged across the rupture depth. The 2.5D modeling approach accounts for the 3D effect of the finite rupture depth, while keeping the computational cost the same as in 2D simulations. This approach is appropriate for large earthquakes whose rupture saturates the seismogenic depth and then propagates horizontally. At any point along the fault strike, the slip in the 2.5D simulation corresponds to the maximum slip of a 3D problem in which the displacement is assumed to have a depth profile $s_p(z)$, prescribed as a sine function with wavelength of two times seismogenic depth (Weng and Ampuero, 2019).

We prescribe the medium properties (density, P- and S- wave velocities) and a constant on-fault normal stress. The fault behavior is governed by the slip-weakening friction law (Andrews, 1976), which acts as a boundary condition relating the fault shear stress and slip. It has three parameters: static friction strength τ_s, dynamic friction strength τ_d, and slip-weakening distance D_c, which are allowed to vary spatially along the fault. Additionally, the initial shear stress τ_0 is also heterogeneous and unknown. During the inversion, we assume the dynamic friction to be constant, and invert for three heterogenous dynamic parameters - stress drop $\Delta\tau_d = \tau_0 - \tau_d$, strength excess $\tau_e = \tau_s - \tau_0$, and fracture energy $E_g = \frac{1}{2}(\tau_s - \tau_d) D_c$. We approximate the heterogeneous distribution of the dynamic parameters as piecewise linear distributions, evaluated on the fine simulation grid by linear interpolation between control values that are distributed on a coarser regular grid. As the goal is to model very large earthquakes on faults that are hundreds of kilometers long, we set the coarse grid spacing to 10 km. This spacing is a compromise between the smallest scale of the features we can explore and the computational cost of the inverse problem (which increases rapidly with the number of model parameters).

We keep the size of the spectral element model domain to a minimum necessary for an accurate dynamic simulation. To calculate synthetic seismograms on stations that are often outside this domain, we use the code AXITRA (Cotton and Coutant, 1997). To model seismograms, we expand the 2.5D slip rate solution to a vertical 3D fault, using the assumed depth profile $s_p(z)$. The slip rate at along strike position x and depth z is calculated from the 2.5D slip rate $\dot{s}(x)$ as:

$$\dot{s}(x,z)=s_p(z)\dot{s}(x).$$

This expansion is consistent with the description of the 2.5D approximation in Weng and Ampuero (2019). The main approximation in comparison with a fully 3D dynamic model is that we assume the depth profile of slip is the same all along the fault.

3.2 Dynamic Inversion

We developed a new dynamic earthquake source inversion package PT-MCMC_seis, based on the PT-MCMC code (see Resources), the code is written in the Python programming language, using MPI to handle the communication between parallel chains. The communication between the MCMC algorithm and the forward model code is conveniently handled through the input/output files. Sem2Dpack and AXITRA can be thus exchanged for a different, more complex code with only minor changes in the handling of the files.

The Metropolis-Hastings algorithm is based on proposing the candidate for the $n+1$ member m'_{n+1} of the Markov chain, based on randomly varying the n-th member m_n.

The efficiency of the MCMC sampling can be improved by combining a mix of different algorithms for the random proposals (Tierney, 1994). In every Metropolis-Hastings step the proposal algorithm is randomly chosen according to a chosen ratio. The PT-MCMC package had several commonly used proposal algorithms already included, we expanded it by adding the log-normal perturbation.

In our inversion, we employ two proposals: (1) log-normal random perturbation (Gallovic, 2019) and (2) differential evolution step (Cajo, 2006). The log-normal step,

$$m'_{n+1}=m_n+\delta_{\ln}\exp[-\log(r)],$$

produces samples from a log-normal distribution with random real number r from a uniform distribution between 0 and 1. The parameter $\delta_{\ln}$ controls the size of the step.

The differential evolution proposes the candidate based on a historical distribution of models. From a buffer of N last members of the chain, we choose two random members f_j and f_k and construct the candidate as:

$$f'_{n+1}=f_n+\delta_{DE}(f_j-f_k).$$

The parameter δ_{DE} controls the size of the step.

3.3 Two-Stage Inversion

The training of WGAN requires a sufficiently large dataset, covering the extent of the prior PDF. Depending on the dimension and complexity of the PDF, this sample size ranges from hundreds or thousands (Patel et al., 2022) to hundreds of thousands in the case of image generation applications (Saxena and Cao, 2022). The acquisition of such a training set for dynamic earthquake rupture models is a challenge because databases of dynamic models of past earthquakes are rarely available. To create this training dataset for WGAN prior, we aim to use MCMC sampling of an easier problem, optimally one with both lower dimension and less computational demand.

We present a multi-stage Bayesian inversion, taking advantage of unique properties of the dynamic earthquake rupture forward problem. The rupture of a large earthquake nucleates on one point of the fault, the nucleation area, then propagates away from it. Reverse-propagation of the rupture or re-activation of already ruptured segments happens only rarely. We can thus divide the earthquake rupture (see Figure 2 for illustration) into a hierarchy of temporal and spatial windows (e.g. window 1 is 0-10 s and 0-100 km, window 2 is 10-20 s and 0-200 km, etc). The initial inversion stage focuses on the first rupture window; it has fewer model parameters and a less costly forward problem. Inversion stages are interdependent: earlier stage inversion results act as a prior for a later stage inversion. We train a GAN on the samples of dynamic model parameters obtained in an earlier stage inversion, and use it in the next inversion stage to propose dynamic model parameters on the portion of the fault covered by the earlier stage. In this way the GAN output approximates the prior information constrained by the earlier stage inversion.

While the proposed multi-stage approach can be used to divide the dynamic earthquake inversion into multiple stages, we focus here on a proof-of-concept two-stage inversion. We present a simplified scheme of the two-stage inversion in Figures 2a and 2b.

We show the division of a specific dynamic rupture model (used also in Section 4) into two temporal and spatial stages in Figure 2a. The first stage covers the central portion of the fault from -25 to 25 km and contains independent model parameters in 5 control points. Its forward model is less computationally demanding due to the smaller size of the space and time domain (50 km and 9 s vs 100 km and 25 s). Owing to the lower computational demands and lower dimension of the inverse problem, we can expect that it converges and samples its posterior PDF faster than the inversion of the whole model. We expect the second-stage inversion, covering the whole fault, to converge and sample the posterior PDF faster than a whole-model inversion, because a portion of the parameters is better constrained from the first-stage inversion and the dimension of the problem is also lower.

In the first-stage inversion, we start from a wide and uniform prior PDF $p(m)$, similarly to Gallovic et al. (2019). The prior PDF of model parameters are mutually independent. We split the model parameters into two groups, m' and m'' (red and black dots, respectively, in Figs. 2a and 2b). The group m' covers the central portion of the fault, symmetrically around the hypocenter, and will be inverted in the first stage. Assuming the first-stage section of the fault does not rupture again at later times outside the first-stage time window, the dynamic model parameters m' should be well constrained by the first-stage inversion. We can estimate what portion of the seismic data is generated by the first-stage model based on both travel time curves and inspecting seismograms generated by handcrafted models. We use this limited dataset d' (the beginning portions of the seismograms) in the first-stage inversion, leaving out the rest of the dataset d'' containing both later portions of the seismograms and static GPS data. The first-stage inversion consists of the Bayesian update of the prior $p(m')$ based on data d':

$$p(m' \vee d') = k'^{-1} p(d' \vee m') p(m').$$

The second-stage inversion updates the PDF of all model parameters $m = [m', m'']$ based on all available data $d = [d', d'']$. The prior of the second stage is a combination of the first stage posterior PDF and the original wide prior for the rest of the parameters:

$$p(m) = [p(m' \vee d'), p(m'')].$$

The Bayesian update of the whole earthquake can be written for the 2-stage inversion as

$$p(m \vee d) = k^{-1} p(d \vee m)[p(m' \vee d'), p(m'')],$$

where $[p(m' \vee d'), p(m'')]$ signifies a mixed prior of uniform, independent, prior PDF $p(m'')$ and 1st stage posterior $p(m' \vee d')$ that already includes the mutual interdependence of model parameters. The major advantage of this approach is that $p(m' \vee d')$ is more constrained, including the mutual relationships between the dynamic parameters, leading to a much smaller parameter space to explore during the 2nd stage dynamic inversion. We need to take into account that the posterior PDF in both stages are approximated by the MCMC sampling via finite length MCMC chains. Additionally, the prior PDF $p(m')$ in the second stage is further approximated as the output of the generator trained on the first-stage inversion samples of $p(m' \vee d')$.

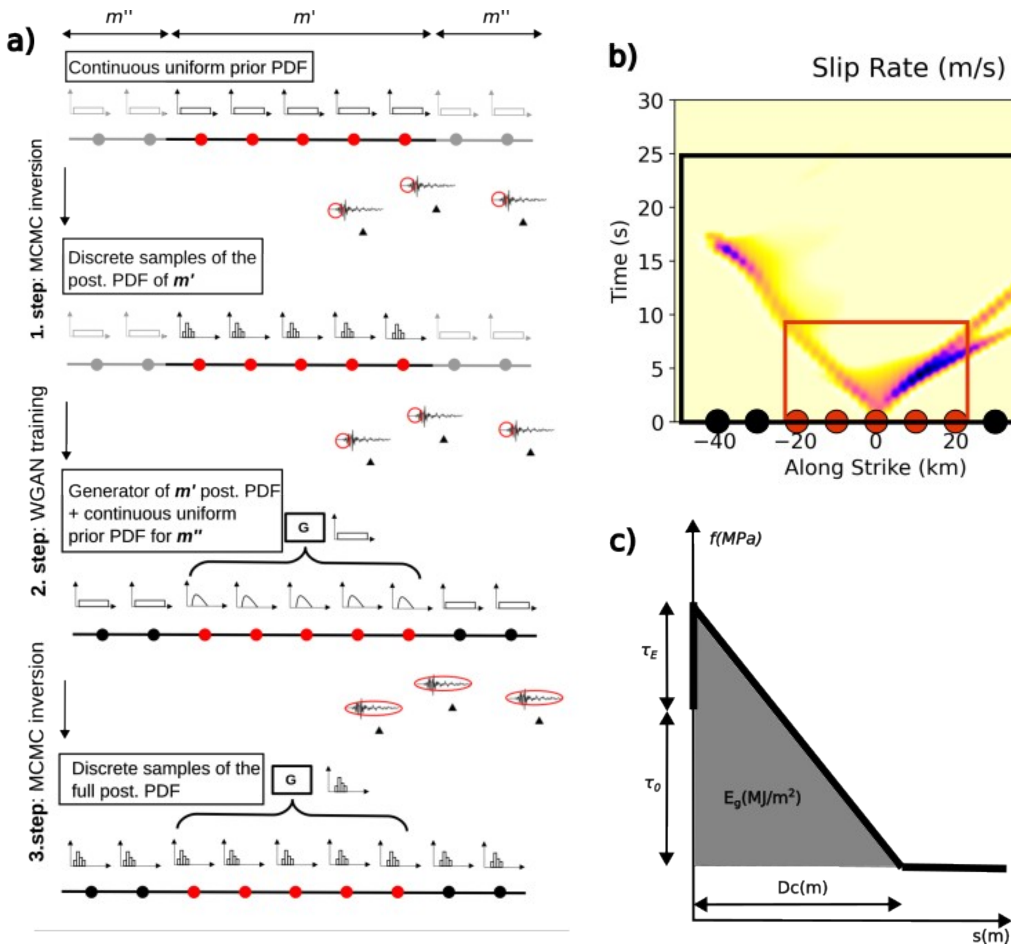

FIGURE 2: two-stage dynamic inversion method: (a) Illustration of the 2-stage dynamic inversion method steps. The thick black line with red and black dots represents the discretized fault, with nodes where model parameters are set. The triangles and seismograms represent measured data. Red nodes with model parameters included in the subset m' are constrained from the beginning portions of the seismograms during the 1-st stage inversion (1.step), leading to a set of discrete samples from the posterior PDF. In the second step, we interpolate between the samples by training a generator G that maps its latent space to the model parameter space. The third step consists of a 2-nd stage inversion, constraining both the generator latent inputs and the m'' subset of model parameters to create a database of discrete samples of the posterior PDF constrained by all available data. (b) Division of the slip-rate distribution of a dynamic model into two-stages, in both time and space. The 1st stage extent is represented by a red rectangle in space-time and red points representing model parameter nodes, while the 2nd stage extent is represented by the black rectangle and black nodes. (c) The slip-weakening friction law relating fault slip and shear stress.

4 Description of the Synthetic test and Results

We present a synthetic dynamic inversion test to compare the performance of the classical PT-MCMC dynamic inversion and our 2-stage PT-MCMC dynamic inversion. We designed a dynamic earthquake model by prescribing handcrafted values of the dynamic parameters on a 100 km long fault and running a 2.5D dynamic rupture simulation. Using the resulting source model, we simulate data by computing low-frequency seismograms and GPS displacements at 12 points along the fault (see Figure 3a for the positions with respect to the fault). We then apply both inversion approaches to sample model parameters that explain the simulated data.

While we use a handcrafted forward model with known dynamic parameters as a ground truth, the inverse problem is still highly non-unique and the shape of the posterior PDF is unknown and could contain multiple maxima. First, we assess if the inversion method finds the maximum around the handcrafted model, i.e. if the ground truth dynamic parameters are found to have relatively high posterior PDF values. Next, we evaluate properties of the inversion methods that are important for practical use, mainly: the integrated autocorrelation time, which controls how many independent samples of the posterior PDF are generated, and the variability of the results between several MCMC runs, both in the dynamic parameters and the kinematic ones.

The PDFs presented in this section are often strongly non-Gaussian. To better display the shapes of the PDFs we show their kernel density estimates (KDE) defined as (Rosenblatt, 1956; Parzen, 1962) :

$$\hat{f}(x)=\frac{1}{nh}\sum_{i=1}^{n}K\left(\frac{x-x_i}{h}\right),$$

where n is number of points, h a smoothing parameter, x_i the i-th sample from the PDF and K a Gaussian kernel function. We use the standard Scott's rule to set the value of the smoothing parameter $h=N_p^{-1/(d+4)}$, where N_p is number of samples and $d=1$, dimension of the function.

4.1 Description of the test

As described in Section 3.1, we parametrize the distribution of the dynamic parameters as piecewise linear distributions along the fault controlled by values on a regular grid of control points with 10 km spacing (dots in Figure 3a). The model parameters to be inverted for are the values of stress drop, strength excess, and fracture energy at these control points. The control grid starts 10 km along strike, ends at 90 km, and contains 9 control points in total, leading to 27 model parameters. At the edge of the fault, outside of the control grid, we set high values of fracture energy and strength excess together with low stress drop to act as a barrier stopping the rupture. The forward simulations use a much finer grid, on which dynamic parameters are linearly interpolated between the values of the coarse control grid. We nucleate the earthquake at the center of the fault (50 km along strike) by prescribing time-weakening that enforces a rupture front expanding at 2 km/s during 2 seconds. The friction coefficient drops from 0.585 to 0.4 in the nucleation zone.

We prepare a target dynamic model that nucleates in the center of the fault (50 km along strike) and ruptures the whole fault. We show the model parameters, along strike distributions of slip-rate and slip in Figures 3c and 3d. The slip rate distribution in space and time is shown in Figure 3e. The eastward rupture (0-50 km along strike) propagates at supershear speed, while the westward rupture speed is subshear.

We generate strong motion displacement seismograms in the frequency band 0.05-0.5 Hz at 12 seismic stations and coseismic GPS displacements at 12 GPS stations. Their locations are shown in Figure 3a. We prescribe a Gaussian distribution of seismogram and GPS error with 15 cm and 2 cm standard deviation, respectively. The likelihood function is thus based on the L^2 norm of the difference between the target and synthetic data of both seismograms and GPS displacements, normalized by the standard deviation of their error.

We apply PT-MCMC_seis to sample the posterior PDF. For the direct inversion, we run 5 independent dynamic inversions for 25,000 steps. For the two-stage inversion, we first run 3 first-stage inversions and construct a GAN prior out of their pooled samples. Then we run 5 independent second-stage inversions under the same conditions as the direct (single-stage) inversions. In all cases, each inversion uses 12 chains with temperatures geometrically distributed between 1 and 30. Each inversion thus visits 300,000 models. We choose an initial model for the inversion by randomly perturbing the ground-truth dynamic parameters by up to 5%.

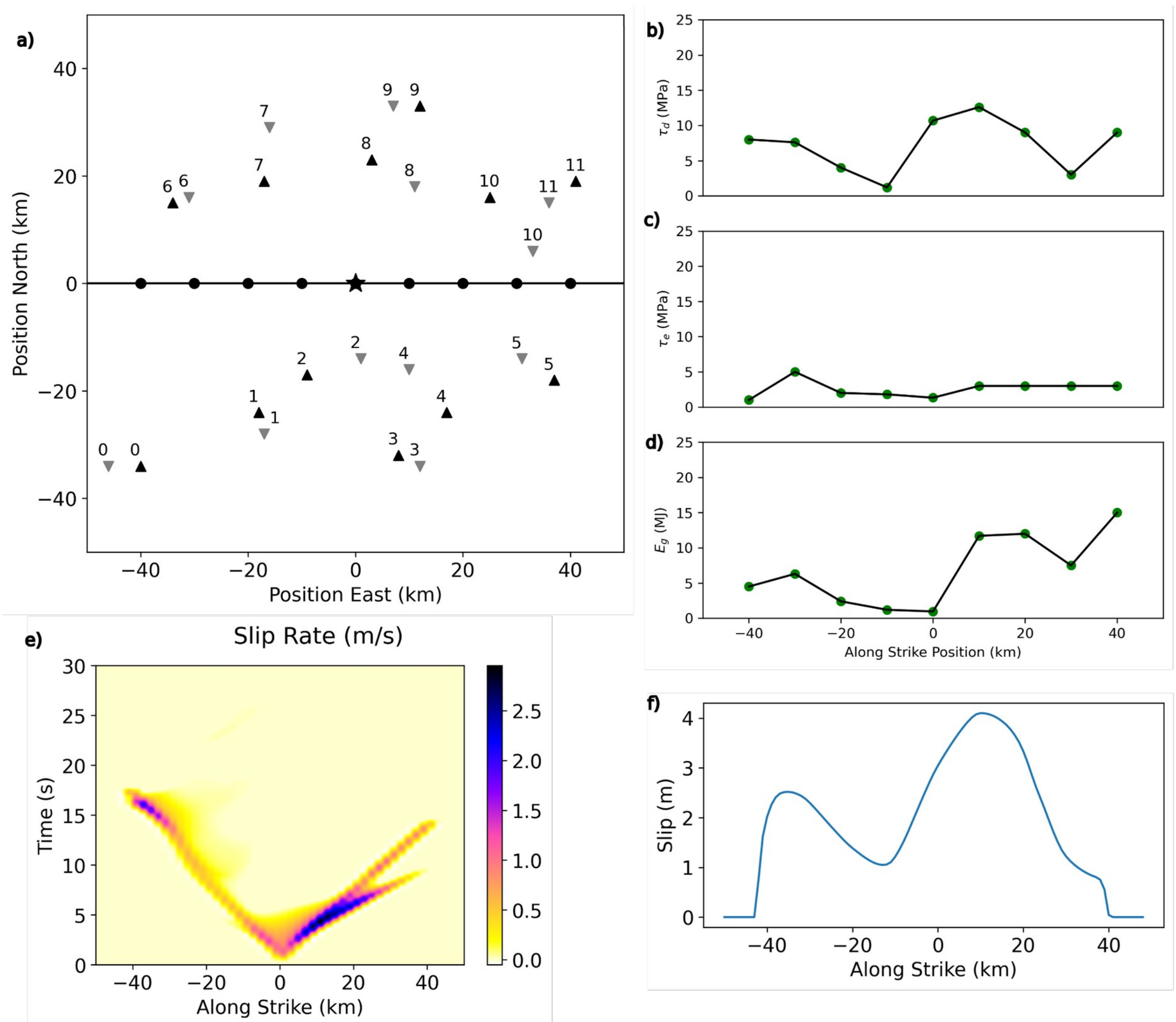

FIGURE 3 Problem setup and target model: (a) Map of the test model fault geometry including model parameter nodes (black circles), seismic stations (black triangles), GPS stations (gray upside-down triangles) and the nucleation zone (black star). Along-strike distribution of the dynamic parameters (stress drop (b), strength excess (c), and fracture energy (d)) with model parameter node values displayed as green circles and the linear interpolation between them as black lines. (e) Slip-rate (e) and slip (f) distributions of the target dynamic model.

4.2 Two-stage inversion details

The extent of the first-stage model is 60 km along strike and 9 s in time (see Figure 2a). We invert for the dynamic parameters at the 5 control points located from -20 km to 20 km along strike, for a total number of 15 model parameters. We chose to fit strong-motion seismograms over a limited time window, with durations ranging from 8 s for the station furthest from the nucleation to 18 s for the station closest to the nucleation. We show seismogram data and their fit by the inversion in Figure S1. The computational demands for one first-stage forward simulation are decreased by 75% in comparison with the full-scale simulation, while the dimension of the problem is 55% of the whole.

The first-stage inversion consisted of 3 independent MCMC runs. Their average IAT is 518 +- 151 (the large error is caused by one run having an IAT of over 700). We removed the first 2000 samples as a burn in period and undersampled by a factor of 60, which led to a training dataset of 1100 models. We chose the undersampling factor of 60 as the training process with smoother (less undersampled) dataset was easier and allowed the WGAN algorithm to more easily generalize between the samples. This undersampling was also sufficient to remove any redundant models stemming from the refused proposals in the Metropolis-Hastings algorithm. The posterior PDF of the model parameters is shown in Figures 4a,b,c, calculated as 1D kernel density estimates from the same training dataset.

We experimented with various setups of the critic and generator architecture and metaparameters of the training process. We chose to use an architecture based on fully connected neural networks with 2 internal layers for the generator and 3 for the critic. All internal layers consist of 128 neurons with a rectifier activation function (ReLu). The original WGAN/WGAN-GP uses convolution layers for image generation applications. The difference in our case is a much lower dimension of the problem/output of the generator (3 x 5 parameters vs 28 x 28 in the MNIST dataset (Deng, 2012)). Using convolution layers can be more advantageous in problems with finer discretization of parameters.

We use the Adam optimizer to train both networks, with batch size of 16, learning rate of 0.0001, and metaparameters $\beta_1 = 0.9$ and $\beta_2 = 0.999$. We set a three-dimensional latent space for the generator and set the PDF distribution of the latent vectors as a 3D Gaussian function with mean of 0.5 and standard deviation of 0.33, truncated to the interval [0,1]. The training process took 4 million steps to achieve convergence in the cost function of both generator and critic (see Figure 4d). The generator can be then used as a prior in the second stage inversion as it generates samples (sets of model parameters) whose distribution closely approximates the distribution of the training set (see Figure 6a,b,c for the generated prior PDF).

The second-stage inversion involves the same forward model as the whole inversion. The parametrization of the problem is different: the second-stage inversion inverts for 4 x 3 dynamic parameters outside the first-stage portion of the fault and for the 3-dimensional latent space vectors of the generator associated with the first-stage portion of the fault. The total number of model parameters in the second stage is thus 15 instead of 27 in the direct inversion.

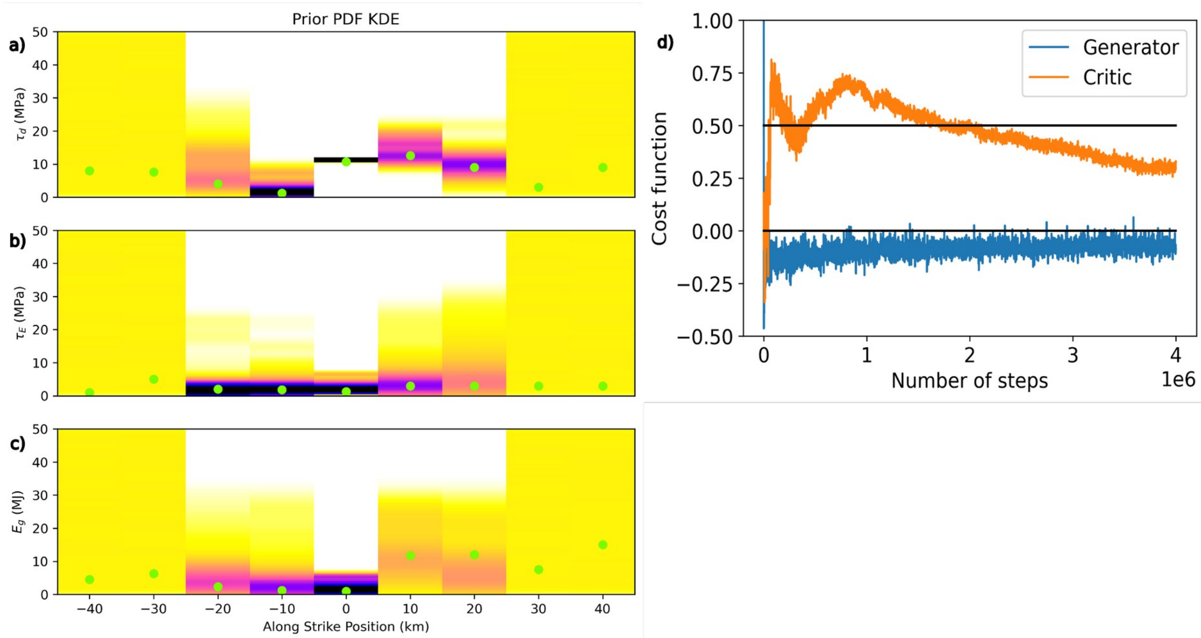

FIGURE 4: 1-st stage inversion result and training of WGANs: Heat map showing 1D kernel density estimates (KDEs) of dynamic parameters along the fault: stress drop (a), strength excess (b) and fracture energy (c). Green dots denote target model parameters and purple dots and error bars show mean and standard deviation of the posterior PDF.(d) Generator (blue line) and Critic (orange line) cost function values as a function of the number of training steps.

Inversion type	Spatial dimension	Time dimension	CPU time	Burn-in period	IAT (steps)	Acceptance T=1	Acceptance of exchange
Direct	100 km	30 s	42 s	5000 steps	426 +- 65	0.23+-0.01	0.24+-0.01
1st stage	60 km	9 s	9 s	3000 steps	518 +- 151	0.40+-0.01	0.28+-0.01
2nd stage	100 km	30 s	42 s	5000 steps	339 +- 81	0.13+-0.01	0.28+-0.01

TABLE 1 Details of the inversions: Table includes important numerical (spatial and temporal dimension) statistical properties (Integrated autocorrelation time, acceptance rates) of the direct and both stages of the two stage inversion.

4.3 Results

We present the average acceptance rates of chains with lowest and highest temperature and an average acceptance rate of the temperature swaps in Table 1. We show KDEs of prior and posterior PDFs of dynamic parameters in Figures 5 and 6 for the direct and second stage of the 2-stage inversion, respectively. These are pooled results of all 5 runs of either direct or two-stage inversions as would be done during the application of dynamic inversion to study a specific earthquake. We present the single plots for each inversion in the Supplement to show differences between single MCMC runs.

We present properties of the MCMC inversions, namely IAT and acceptance rates, in Table 1. To illustrate the properties of the direct and two-stage inversion methods, we include the estimates of the dynamic parameters (Figure S5) and kinematic parameters (Figure S6) from single MCMC runs. The estimates are calculated as an average from a model set acquired from the Markov chain by removing the burn-in period and undersampling by a factor of 2 x IAT. In Figure 7, we show the histograms of the ratios between the variances of estimates of both dynamic and kinematic parameters.

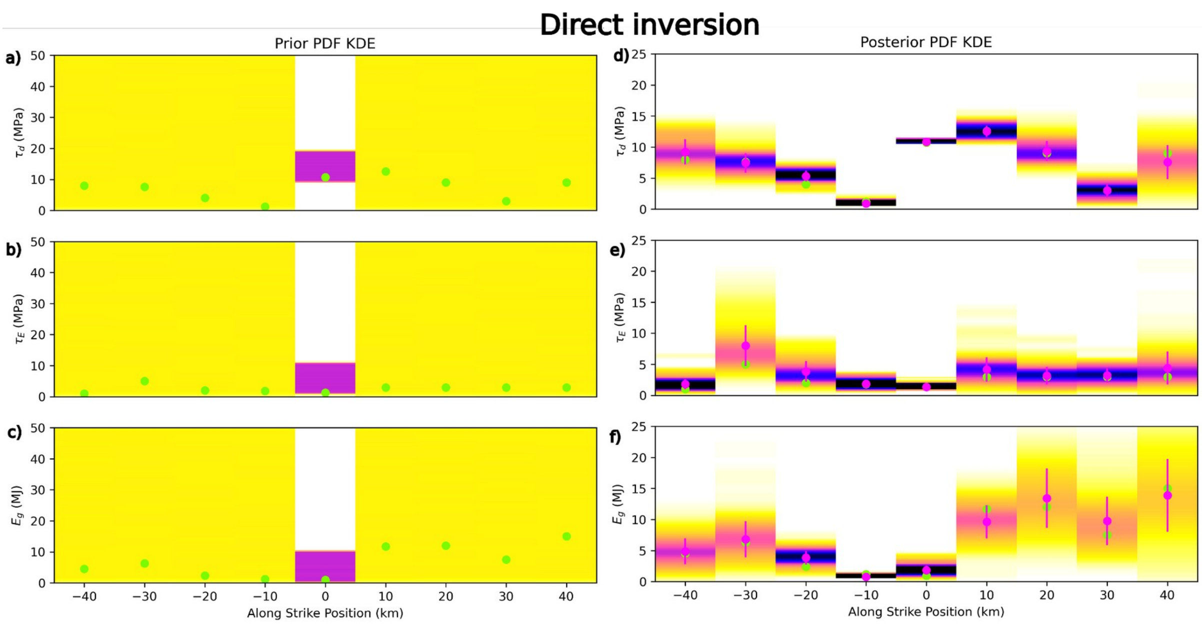

FIGURE 5 1D KDEs of dynamic parameter prior and posterior PDF of direct inversion**:** *Heat map showing 1D kernel density estimates (KDEs) of prior (a,b,c) and posterior (d,e,f) PDF of dynamic parameters from direct dynamic inversion, showing stress drop (a,d), strength excess (b,e) and fracture energy (c,f) along the fault. Green dots denote target model parameters and purple dots and error bars in (d,e,f) show mean and standard deviation of the posterior PDF.*

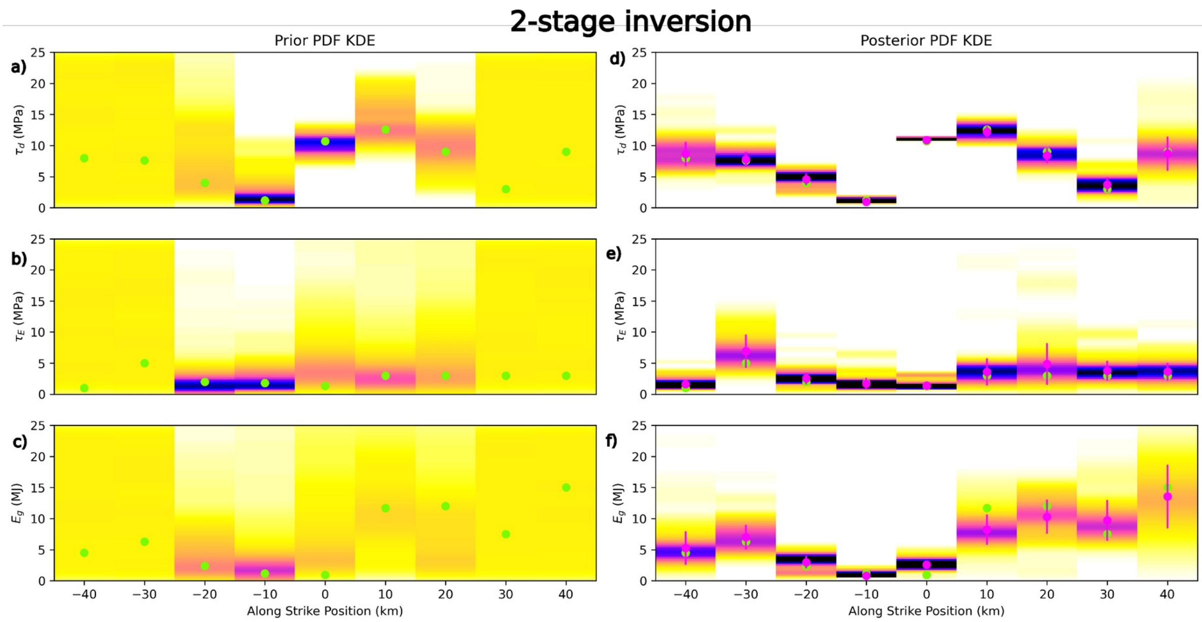

FIGURE 6 1D KDEs of dynamic parameter prior and posterior PDF of the second stage of the 2-stage inversion: *Heat map showing 1D kernel density estimates (KDEs) of prior (a,b,c) and posterior (d,e,f) PDF of dynamic parameters from the second stage of the 2-stage dynamic inversion, showing stress drop (a,d), strength excess (b,e) and fracture energy (c,f) along the fault. Green dots denote target model parameters and purple dots and error bars in (d,e,f) show mean and standard deviation of the posterior PDF. Prior PDF of the 1-stage parameters (-20 to 20 km along strike) is generated by WGAN.*

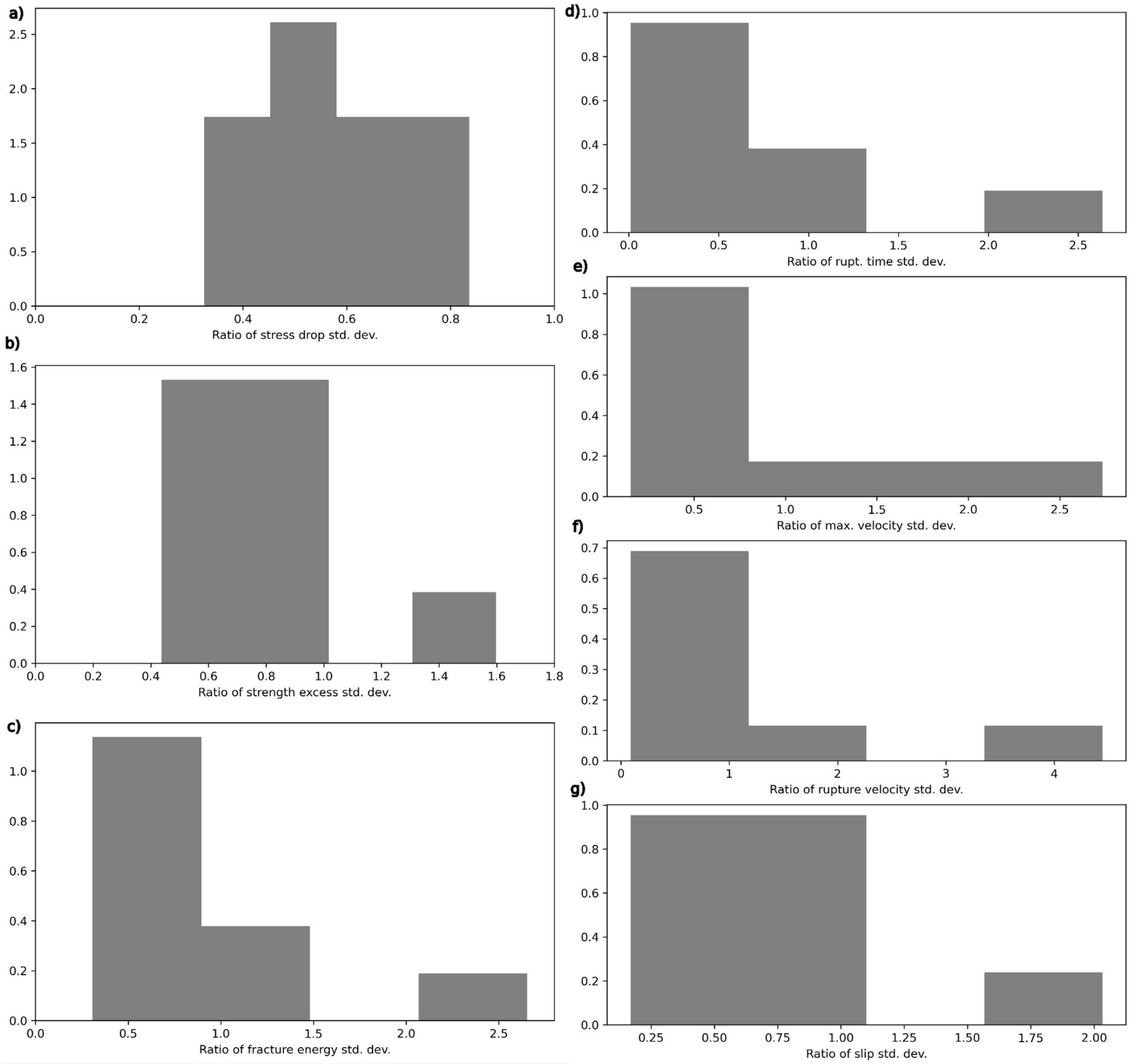

FIGURE 7: Ratios of expectancy variances of dynamic and kinematic parameters: *Distribution of ratio between normalized standard deviation of mean estimate from 2-stage and direct inversion (values less than one mean lower standard deviation of 2-stage results) of (a) stress drop, (b) strength excess, (c) fracture energy, (d) rupture time), (e) maximum velocity, (f) rupture velocity, and (g) slip.*

6 Discussion

We performed a Bayesian dynamic earthquake source inversion of a target model and compared the performance of the original MCMC dynamic inversion with our newly developed two-stage approach.

We include results of 5 independent inversion runs for each method, for the first time assessing the stability and repeatability of the dynamic inversion results. We parametrize the performance and efficiency of the methods by the integrated autocorrelation time (IAT) and the variance between both dynamic and kinematic properties of the rupture across different inversion runs.

The IAT values reported in Table 1 demonstrate the difficulty of the dynamic inversion problem and motivate our new method. Indeed, with IAT in the range of 400, the direct dynamic inversion produces only ~20-30 independent samples from the posterior PDF after visiting 300,000 models. This result underscores the need for further improvements of the dynamic inversion methodology. Our novel two-stage inversion method is a step in that direction: it has a 20% lower IAT than the direct inversion. Note that the reported IAT is a maximum over all model parameter dimensions; its value is driven by model parameters with high uncertainty that tend to be at the edges of the rupture, e.g. the stress drop at -40 and -30 km along strike and the fracture energy at 30 and 40 km along strike. The volume of this subset of the parameter space is not decreased by our two-stage method, which ultimately limits the improvements on sampling speed. The IAT calculated as mean over all parameter dimensions reaches 178+-19 and 152+-34 for the direct inversion and 2-stage inversion, respectively. Comparison of the distributions of the IAT for all model parameters (see Figure S8) shows a consistent improvement for the 2-stage method in limiting the size of the tail at large values of IAT.

The decrease in variance of both dynamic and kinematic parameters (Fig. 7) is more significant: the majority of the standard deviations of both dynamic and kinematic parameters estimates are lower for the 2-stage method. In many cases, more than half of the parameter estimates show a 50% improvement in the standard deviation (especially strength excess in Fig 7b and rupture time in Fig 7d). This points towards better reliability of the new two-stage MCMC approach. The improvement is very visible even at the edges of the rupture not covered by the first-stage prior. Especially, the variance of kinematic parameters on the eastern portion of the fault (Figure S4b), which is less covered by data, is much larger in the direct inversion than in the two-stage inversion, e.g. rupture time variance of 35% versus less than 5%.

One of the manifestations of the non-uniqueness of the dynamic inversion problem are trade-offs between dynamic model parameters. We calculated correlations between all model parameters (Figure 8a). In Figure 8b, we point out very clear correlations between fracture energy and stress drop, both on the subshear and supershear portions of the fault. This relationship is weaker at the nucleation zone and at the edges of the fault, where rupture arrests. This trade-off is expected based on analytical results from the 2.5D theory of subshear elongated ruptures (Weng and Ampuero, 2019). This theory establishes a rupture tip equation of motion that relates the evolution of rupture speed and rupture acceleration to the ratio of fracture energy and static energy release rate E_g/G_0. That structure of the equation of motion shows that large subshear ruptures are controlled by the energy ratio E_g/G_0. Given $G_0 = \tau_d^{\,2} W'/\mu$, where W' is a measure of rupture width and μ is shear modulus, the energy ratio is proportional to $E_g/\Delta\tau_d^{\,2}$. The rupture behavior, during subshear portions, should thus depend on the ratio of dynamic parameters $E_g/\Delta\tau_d^{\,2}$ and we should expect the trade-off between fracture energy and stress drop. We note that, although this theory is so far available only for subshear ruptures, our results suggest that the trade-off between fracture energy and stress drop generalizes to supershear ruptures too.

We did not encounter any other consistently occurring local tradeoffs between parameters, but we also observe anticorrelation between values of both stress drop and fracture energy among neighboring control points (see Figure 8a). As stress drop correlates with slip and therefore with the earthquake magnitude, we explain this trade-off by the need to match the earthquake magnitude.

We note that the posterior PDF shapes are influenced by the properties of the dataset, both in terms of frequency, station amount and locations. In particular, the closer are the seismic stations to the fault, the better resolution of the rupture velocity as the arrival times at the stations are closer to rupture times on specific segments of the fault. Additionally, the inclusion of the static GPS data significantly decreases the uncertainty as the static displacement strongly constrains the amount and position of slip and stress drop.

While the Parallel tempering method uses several parallel chains, only one chain samples the posterior PDF. The other chains sample the tempered distributions. We can better utilize modern supercomputers to increase the number of posterior PDF samples by running several independent dynamic inversions in parallel. Running the inversions independently requires expending additional computational resources on the separate initial burn-in periods.

We note that our synthetic test represents an optimal situation in which the target model is known and the initial guess is only 5% away from the target, with a burn-in period of 5000 steps (60000 visited models, or 20% of the total MCMC steps and visited models). Based on our experience, it can be expected that inverting a real earthquake will require a higher percentage of the total to be expended for the exploratory burn-in period. For example, in Schliwa et al. (2024), 1.2 million models were visited during the exploratory stage and 0.8 million during the sampling stage (40% of the total).

With increasing number of parallel runs, the speedup from this naively parallelized MCMC inversion tends towards $1+1/\gamma$, where γ is the fraction of samples removed as a burn-in period (Wu et al., 2012). The advantage of our 2-stage approach is that the computationally more demanding second stage already starts with a PDF of the portion of the parameters significantly constrained, thus decreasing the length of the burn-in stage and increasing the efficiency of the parallelization. Additionally, the burn-in period for the faster first stage inversion is shorter, thus making its parallelization more efficient.

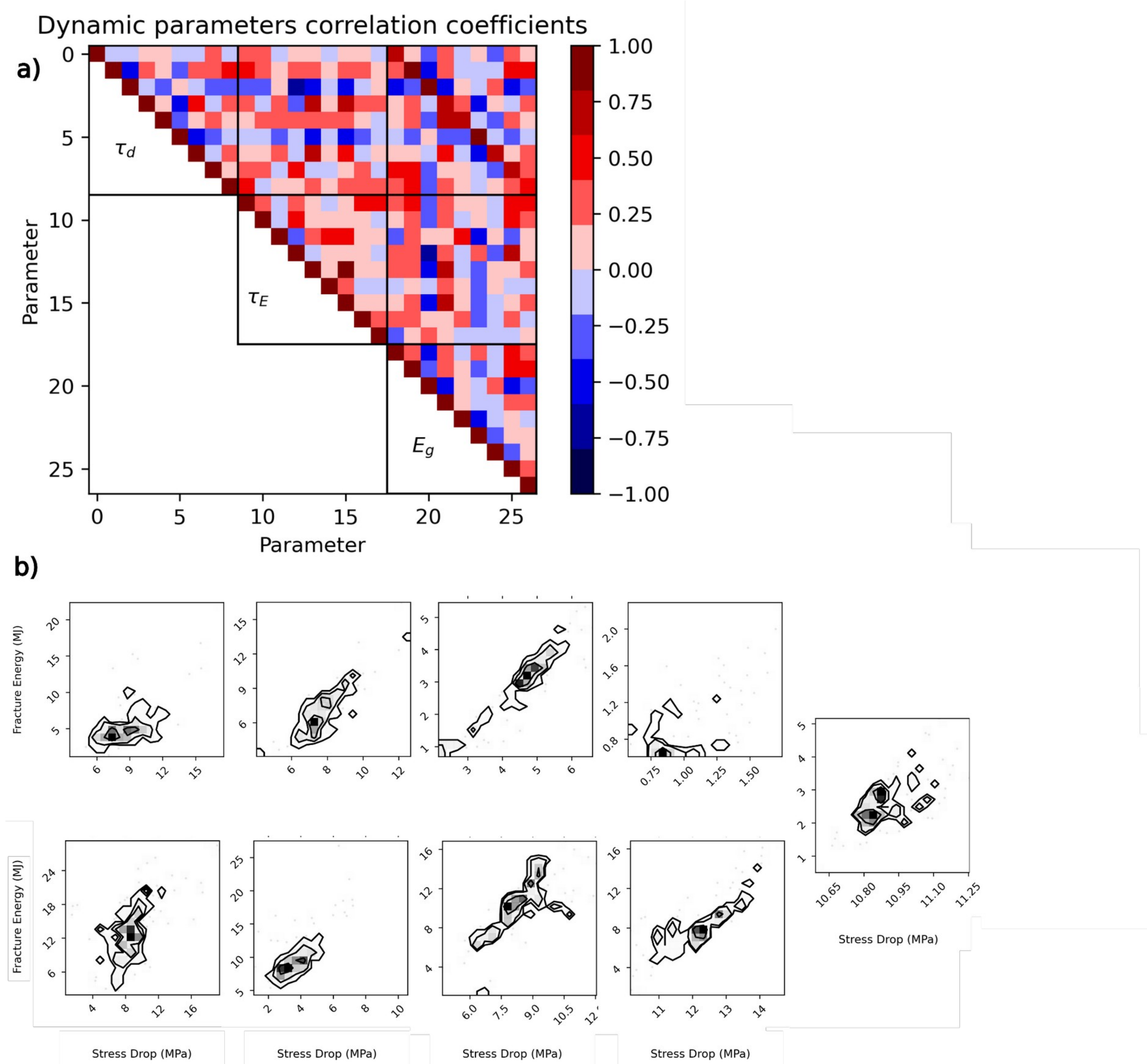

***Figure 8**: **Correlations of dynamic parameters:** (a) Matrix of correlation coefficients between the dynamic parameters. Red values denote a positive correlation, while blue values denote a negative correlation. The first 9 columns correspond to stress drop (from -40 to +40 km along strike), the next 9 to strength excess and the last 9 to fracture energy. (b-j) Correlation graphs of stress drop and fracture energy at positions from -40 to 40 km along strike.*

7 Conclusion

We presented and tested a novel multi-stage approach for dynamic earthquake source inversion, based on dividing the earthquake rupture into hierarchical temporal and spatial stages, with information about parameters in the earlier stages acting as a prior for the later stages. This approach is made possible by employing Wasserstein Generative Adversarial Networks, trained on the earlier stage inversion results, to make proposals of the model parameters. We show a proof-of-concept dynamic inversion of a synthetic benchmark, comparing the performance of direct Monte Carlo dynamic inversion with parallel tempering to that of our two-stage approach. We show an improvement in relevant performance metrics, including integrated autocorrelation time, and show a large increase in stability of the inversion across 5 independent runs.

The new multi-stage approach has a potential to improve the workflow of Bayesian dynamic earthquake source inversion, where the set up of an initial model with high enough posterior PDF is both computationally and work intensive. This is alleviated by the multi-stage approach that reduces the number of model parameters and data at each stage. In combination with presented performance and reliability improvements the multi-stage approach can be a next step in tackling the difficult task of nonlinear inversion of physics-based earthquake models.

Acknowledgments

JP acknowledges support by fellowships from the Interdisciplinary Institute for Artificial Intelligence 3IA Côte d'Azur. The authors declare that they have no competing interests.

Open Research

The software SEM2DPACK is freely available at: https://github.com/jpampuero/sem2dpack. Python software for the dynamic inversion of earthquake source PT-MCMC_seis and the code implementing WGAN training on the posterior PDF from the dynamic inversion is freely available at: https://github.com/JanPremus/PT-MCMC_seis. The original Paralel Tempering library PTMCMCSampler is available at: https://github.com/nanograv/PTMCMCSampler. The key input parameters for running numerical simulations are within the paper and in the example folder at https://github.com/JanPremus/PT-MCMC_seis.

References

Ampuero, J. P., T. W. Currie, M. T. Herrera, Y. Huang, H. Lestrelin, C. Liang, F. Llorens, E. Oral and H. Weng (2024), jpampuero/sem2dpack: SEM2DPACK v2.3.9 (SEM2DPACK_2.3.9). Zenodo. [software] https://doi.org/10.5281/zenodo.13821494

Andrews, D. J. (1976). Rupture velocity of plane strain shear cracks.*J. Geophys. Res.* 81(32), 5679–5687.

Arjovsky, M., Chintala, S. and Bottou, L. (2017). . Wasserstein generative adversarial networks. *Proceedings of the International conference on machine learning*, 214-223

Arridge, S., P. Maass, O. Öktem, and C.B. Schönlieb (2019). Solving inverse problems using data-driven models. *Acta Numer*, 28, 1–174.

Betancourt, M. (2017). A conceptual introduction to Hamiltonian Monte Carlo,preprint (arXiv:1701.02434).

Broberg, K. B., (1998). Crack expanding with constant velocity in an anisotropic solid under anti-plane strain. *Int. J. Fract.*, 93(1), 1–12.

Cotton, F., and O. Coutant (1997). Dynamic stress variations due to shear faults in a plane-layered medium, *Geophys. J. Int.*, 128, 676-688.

Deng, L. (2012). The mnist database of handwritten digit images for machine learning research. *IEEE Trans. Knowl. Data Eng.*, *29*(6), 141–142.

de Souza, V. L. T., B. A. D. Marques, H. C. Batagelo, and J. P. Gois (2023). A review on Generative Adversarial Networks for image generation. *Computers & Graphics*, 114, 13-25.

Duputel, Z., J. Jiang, R. Jolivet, M. Simons, L. Rivera, J.-P. Ampuero, B. Riel, S. E. Owen, A. W. Moore, S. V. Samsonov, et al. (2015), The Iquique earthquake sequence of April 2014: Bayesian modeling accounting for prediction uncertainty, *Geophys. Res. Lett.*, 42, 7949–7957.

Falcioni, M., and M.W. Deem (1999). A biased Monte Carlo scheme for zeolite structure solution, J. Chem. Phys.,110, 1754-1766.

Fichtner, A., A. Zunino, and L. Gebraad (2019) Hamiltonian Monte Carlo solution of tomographic inverse problems, *Geophys. J. Int.*, 216 (2), 1344–1363.

Gabriel, A. A., J.P. Ampuero, L.A. Dalguer, and M. Mai (2013). Source properties of dynamic rupture pulses with off-fault plasticity. *J. Geophys. Res. Solid Earth, 118*(8), 4117-4126.

Gallovič, F., and Ampuero, J.-P. (2015). A New Strategy to Compare Inverted Rupture Models Exploiting the Eigenstructure of the Inverse Problem. *Seismol. Res. Lett*., 86. 1679-1689.

Galvez, P. , J.-P. Ampuero, L. A. Dalguer, S. N. Somala, T. Nissen-Meyer, Dynamic earthquake rupture modelled with an unstructured 3-D spectral element method applied to the 2011 *M*9 Tohoku earthquake, *Geophys. J. Int.*, 198(2), 1222–1240.

Gao, F., and L. Chen (2005). Bayesian or non-Bayesian: a comparison study of item parameter estimation in the three-parameter logistic model. *Appl. Meas. Educ.* 18, 351–380.

Geyer, C.J. (1991). Markov Chain Monte Carlo maximum likelihood. *Computing Science and Statistics: Proceedings of the 23rd Symposium on the Interface*, New York, American Statistical Association, 156-163.

Goodfellow, I., Pouget-Abadie, J., Mirza, M., Xu, B., Warde-Farley, D., Ozair, S., Courville, A. and Bengio, Y. (2014). Generative adversarial nets, *Proceedings of the International Conference on Neural Information Processing Systems (NIPS 2014).* 2672–2680.

Guatteri, M., and P. Spudich (2000). What Can Strong-Motion Data Tell Us about Slip-Weakening Fault-Friction Laws?. *B. Seismol. Soc. Am.* 90 (1): 98–116.

Gui, J., Z. Sun, Y. Wen, D. Tao and J. Ye (2023). A Review on Generative Adversarial Networks: Algorithms, Theory, and Applications. IEEE Trans. Knowl. Data Eng., 35 (04), 3313-3332, 2023.

Gulrajani, I., Ahmed, F., Arjovsky, M., Dumoulin, V., and A. C. Courville (2017). Improved training of wasserstein gans. *Proceedings of Advances in neural information processing systems* 30 *(NIPS 2017)*.

Hallo, M., and F, Gallovič (2016). Fast and cheap approximation of Green function uncertainty for waveform-based earthquake source inversions, *Geophys. J. Int.*, 207(2),1012–1029.

Holden M., M. Pereyra, and K. C. Zygalakis (2022). Bayesian imaging with data-driven priors encoded by neural networks. *SIAM J. Imaging Sci.* 15, 892–924.

Jia, Z., Z. Jin, M. Marchandon, T. Ulrich, A.-A. Gabriel, W. Fan, P. Shearer, X. Zou, J. Rekoske, F. Bulut, A. Garagon, and Y. Fialko (2023) The complex dynamics of the 2023 Kahramanmaraş, Turkey, Mw 7.8-7.7 earthquake doublet. *Science*, 381, 985-990.

Kanamori, H., and E. Brodsky (2001) The Physics of Earthquakes. *Physics Today* 1; 54 (6): 34–40.

Kaneko, Y., N. Lapusta, and J.-P. Ampuero (2008), Spectral element modeling of spontaneous earthquake rupture on rate and state faults: Effect of velocity-strengthening friction at shallow depths, *J. Geophys. Res.*, 113, B09317.

Kantorovich, L.V. (1939). Mathematical Methods of Organizing and Planning Production. Management Science. 6(4), 366–422.

Kurach, K., M. Lučić, X. Zhai, M. Michalski, and S. Gelly (2019). A large-scale study on regularization and normalization in GANs. Proceedings of the International conference on machine learning (PMLR), 3581-3590.

Liu, J. (2001). Monte Carlo Strategies in Scientific Computing. *Springer Texts in Statistics*. Springer New York.

Marschall, M., G. Wübbeler, F. Schmähling, and C. Elster (2023). Machine learning based priors for Bayesian inversion in MR imaging. *Metrologia* 60, 4, 044003.

Metropolis, N., A. W. Rosenbluth, M. N. Rosenbluth, A. H. Teller, and E. Teller (1953). Equation of state calculations by fast computing machines. *J. Chem. Phys.*, *21*(6), 1087-1092.

Minson, S.E. (2024). Cross-fade sampling: extremely efficient Bayesian inversion for a variety of geophysical problems, *Geophys. J. Int.*, 239(3), 1629–1649.

Natesan, P., R. Nandakumar, T. Minka, and J.D. Rubright(2016). Bayesian Prior Choice in IRT Estimation Using MCMC and Variational Bayes. *Front. Psychol*. 7,1422.

Otarola, C., S. Ruiz, C. Herrera, R. Madariaga, C. Siegel (2021). Dynamic rupture of subduction earthquakes located near the trench, E*arth Planet*. Sci. Lett., 562,116842,10.1016/j.epsl.2021.116842.

Parzen, E. (1962). On Estimation of a Probability Density Function and Mode.*Ann. Math. Statist.* 33 (3), 1065–1076.

Patel, D. V., D. Ray, A. A. Oberai (2022). Solution of physics-based Bayesian inverse problems with deep generative priors. *Comput. Methods Appl. Mech. Eng.*, 400, 115428.

Robert, C., and G. Casella (1999). Monte Carlo Statistical Methods. *Springer Texts in Statistics*. Springer New York.

Rosenblatt, M. (1956). Remarks on Some Nonparametric Estimates of a Density Function. *Ann. Math. Statist.*, 27 (3): 832–837.

Salimans, T., I. Goodfellow, W. Zaremba, V. Cheung, A. Radford, and X. Chen (2016). Improved techniques for training gans. Proceedings of the Advances in neural information processing systems, 29.

Sambridge, M. (2014). A Parallel Tempering algorithm for probabilistic sampling and multimodal optimization, *Geophys. J. Int.*, 196(1) Pages 357–374.

Saxena, D., and J. Cao (2022). Generative adversarial networks (GANs): Challenges, solutions, and future directions. ACM Comput Surv, 54(3), 1–42.

Scheiter, M., A.P. Valentine, and M. Sambridge(2024). Bayesian Inference in Geophysics with AI-enhanced Markov chain Monte Carlo. *ESS Open Archive* . October 10, 2024.

Sokal, A. D. (1996). Monte Carlo Methods in Statistical Mechanics: Foundations and New Algorithms; *Cargèse Summer School Lecture Series*; 1996.

Stiernström, V., M. Almquist, and E. M. Dunham (2024). Adjoint-based inversion for stress and frictional parameters in earthquake modeling. J. Comput. Phys., 519, 113447.

Stuart, G. K., S. E. Minkoff, and F. Pereira (2019.) A two-stage Markov chain Monte Carlo method for seismic inversion and uncertainty quantification. *Geophysics* 84 (6), R1003–R1020.

Ter Braak, C.J.F. (2006). A Markov Chain Monte Carlo version of the genetic algorithm Differential Evolution: easy Bayesian computing for real parameter spaces. Stat. Comput., 16(3), 239–249.

Tierney, L. (1994). Markov Chains for Exploring Posterior Distributions. Ann. Statist. 22(4) 1701 - 1728.

Uchide, T., and S. Ide (2007), Development of multiscale slip inversion method and its application to the 2004 mid-Niigata Prefecture earthquake, *J. Geophys. Res.*, 112, B06313.

Uchide, T., S. Ide, and G. C. Beroza (2009), Dynamic high-speed rupture from the onset of the 2004 Parkfield, California, earthquake, *Geophys. Res. Lett.*, 36, L04307.

Uchide, T. (2013), High-speed rupture in the first 20 s of the 2011 Tohoku earthquake, Japan, *Geophys. Res. Lett.*, 40, 2993–2997.

Villani, C. (2008). Optimal transport: old and new, *Springer Science & Business Media*, 338 2008

Weng, H., and J.-P. Ampuero (2019). The dynamics of elongated earthquake ruptures. *J. Geophys. Res. Solid Earth*, 124, 8584–8610.

Wu X. L., C. Sun, T. M. Beissinger, G. J. Rosa, K. A. Weigel, N. de. L. Gatti, and D. Gianola (2012). Parallel Markov chain Monte Carlo - bridging the gap to high-performance Bayesian computation in animal breeding and genetics. *Genet Sel Evol.* 25;44(1):29.

[Journal of Geophysical Research: Solid Earth]

Supporting Information for

Dynamic earthquake source inversion with Generative Adversarial Network priors

Jan Premus[1], Jean Paul Ampuero[1]

[1] Université Côte d'Azur, IRD, CNRS, Observatoire de la Côte d'Azur, Geoazur, Nice, France

Contents of this file

Text S1. Variance of the mean estimate

Here we calculate the error of the MCMC sampling of a random variable *f* (a dynamic source parameter). We assume the chain $\{f_n\}$, $n = 1,2,..N$, is stationary, i.e. its probability distribution is not changing across steps. This property is potentially difficult to meet in practice, but can be approximated by a long enough convergence/exploration period.

The mean

$$M(f) = \frac{1}{N}\sum_{n=1}^{N} f_n \tag{1}$$

is a random variable with variance

$$V[M(f)] = \frac{1}{N^2}\sum_{r=1}^{N}\sum_{s=1}^{N} C^{r,s}(f,f)\sqrt{V(f_r)}\sqrt{V(f_s)} \tag{2}$$

where $C^{r,s}(f,f)$ is the correlation function

$$C^{r,s}(f,f) = M(f_r f_s)/\sqrt{V(f_r)}\sqrt{V(f_s)} \tag{3}$$

Given the process is stationary,

$$\sqrt{V(f_r)} = \sqrt{V(f_s)} = \sigma(f) \tag{4}$$

and thus

$$V[M(f)] = \frac{\sigma^2(f)}{N^2}\sum_{r=1}^{N}\sum_{s=1}^{N} C^{r,s}(f,f)\sqrt{V(f_r)}\sqrt{V(f_s)} \tag{5}$$

The correlation generally decreases towards zero with increasing lag $|r-s|$. Assuming it reaches near-zero values at lags that are small compared to *N*, we approximate the inner sum in (5) as*:*

$$\sum_{s=1}^{N} C^{r,s}(f,f) \approx \sum_{i=-\infty}^{\infty} C^{r,r+i}(f,f) \tag{6}$$

Owing to stationarity, $C^{r,r+i}$ is independent of r, thus we denote it simply by C^i. Noting that the members of the sum over r in Equation (2) are identical and equal to $\sigma^2(f)\sum_{i=-\infty}^{\infty} C^i(f,f)$, we get

$$V[M(f)] \approx \frac{\sigma^2(f)}{N}\sum_{i=-\infty}^{\infty} C^i(f,f) \tag{7}$$

For ‘optimal’ MC, all correlation coefficients except C_0 are 0, and then the variance of the mean estimation is

$$V_{opt}[M(f)] = \frac{\sigma^2(f)}{N} C^0(f,f) \tag{8}$$

For MCMC, we re-write Equation (7) as

$$V_{MC}[M(f)] = \frac{\sigma^2(f)}{N} C^0(f,f) \sum_{i=-\infty}^{\infty} \frac{C^i(f,f)}{C^0(f,f)} \tag{9}$$

For a same number of steps *N*, the variance V_{MC} of MCMC (Eq. 9) is higher than the ideal value V_{opt} (Eq. 8) by a factor defined as twice the *integrated autocorrelation time* (IAT):

$$V_{MC}[M(f)] = V_{opt}[M(f)] \times 2\,\tau_{int}(f) \tag{10}$$

where

$$\tau_{int}(f) = 0.5 \sum_{i=-\infty}^{\infty} \frac{C^i(f,f)}{C^0(f,f)} \tag{11}$$

The factor 0.5 in Equation (11) is only a matter of convention.
The IAT is a measure of the efficiency of the MCMC methods. Equations (8) and (9) show that MCMC with N_{MC} steps achieves the same variance as optimal MC with N_{opt} steps if $N_{MC} = 2\,\tau_{int} \times N_{opt}$. Thus, IAT quantifies how many more steps the MCMC method needs to achieve the optimal variance.
In multidimensional problems with M model parameters, we estimate $\tau_{int}(m_i)$ for each model parameter $m_i, i = 1,2,3, \ldots, M$, separately. The maximum value over all parameters is then taken to evaluate the efficiency of the MCMC method.

Station Number	Window size (s)	Station Number	Window size (s)
0	12.5	6	10.0
1	17.0	7	17.0
2	18.0	8	18.0
3	18.0	9	18.0
4	15.0	10	10.0
5	10.0	11	8.0

Table S1: Time windows lengths for each station in the first-stage inversion of the synthetic test. The start of the window is 2 s before the time of arrival for all stations.

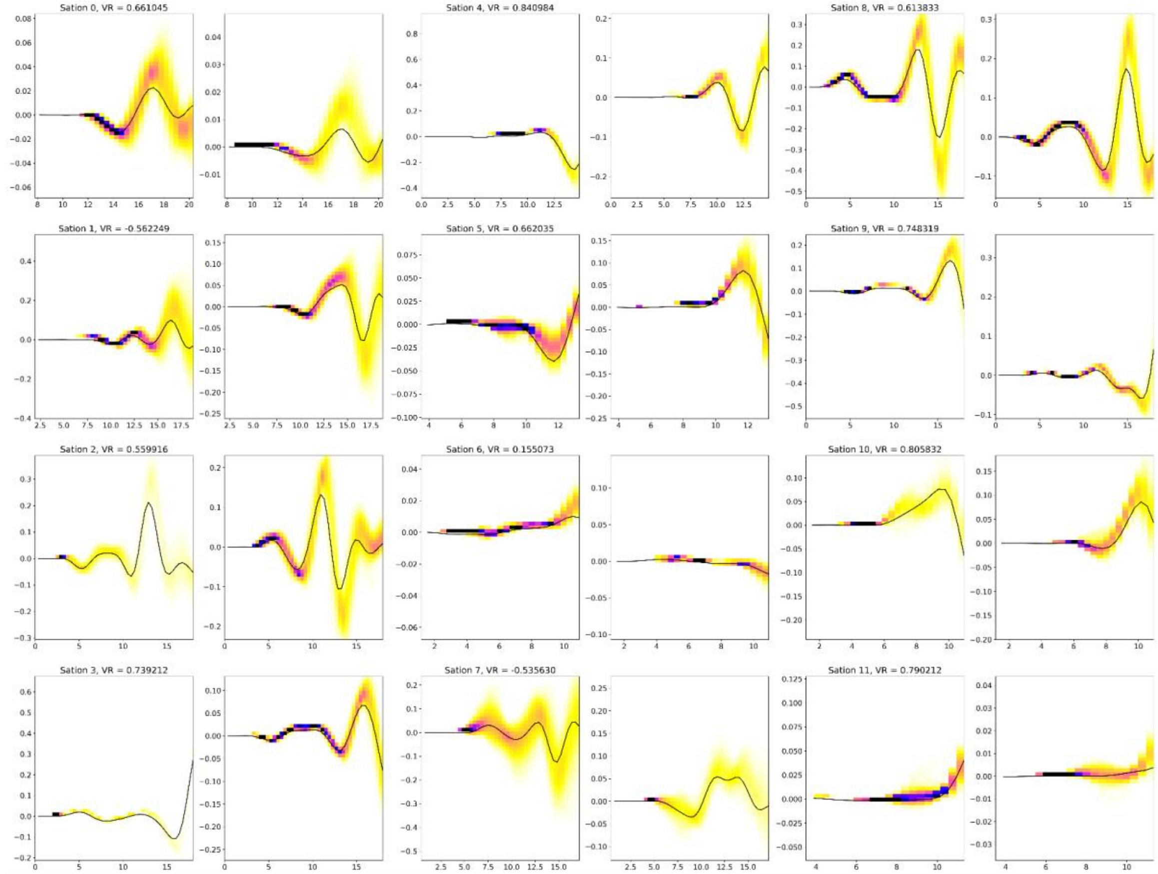

Figure S1: First-stage inversion seismogram fit

Data fit by the first-stage inversion of the initial portions of the seismograms at station locations shown in Figure 3a. Black curves: displacement seismograms. Yellow-red heat map: kernel density estimate of the first-stage inversion seismograms.

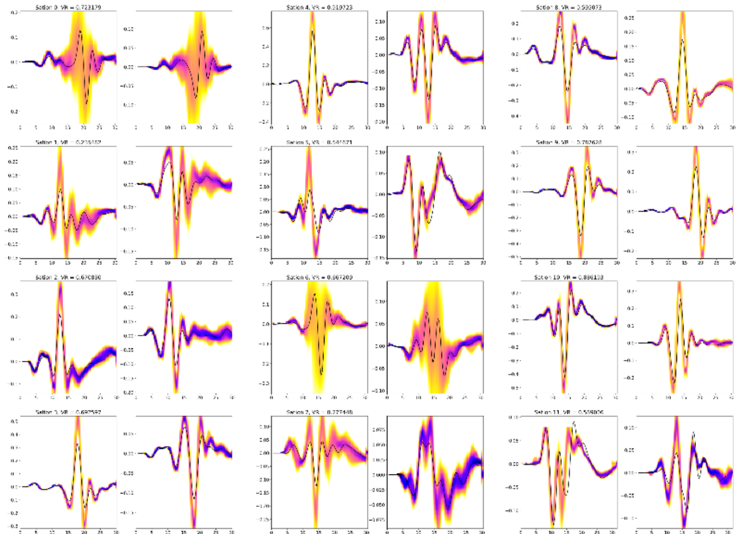

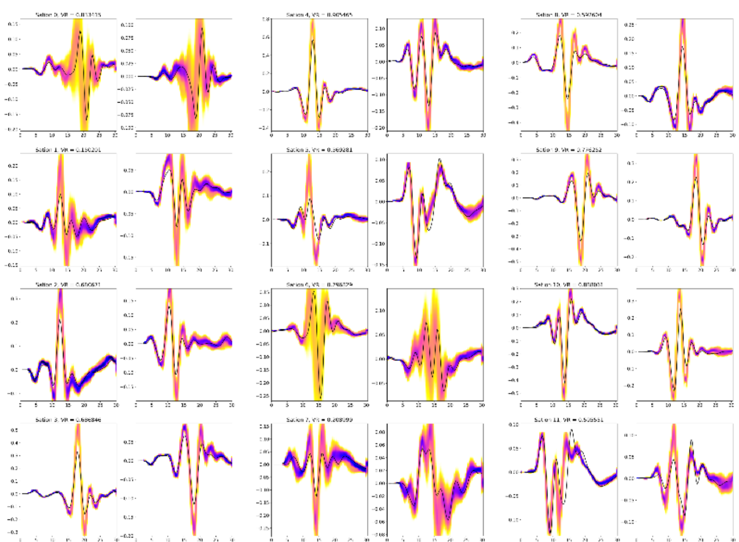

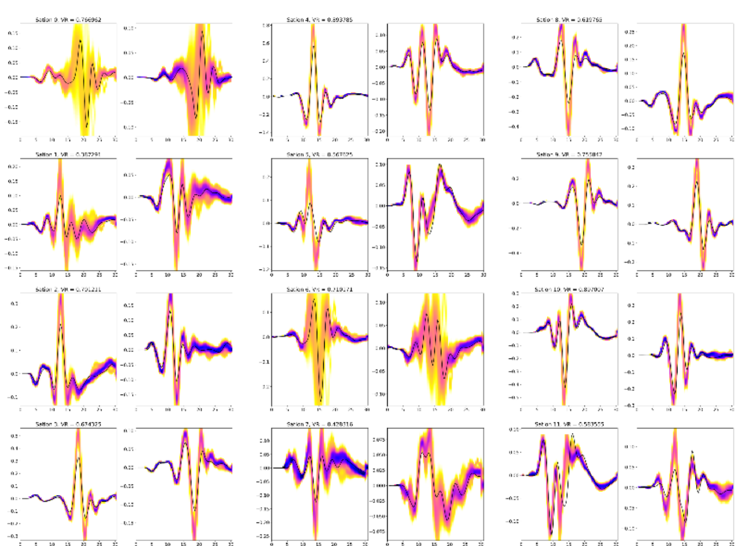

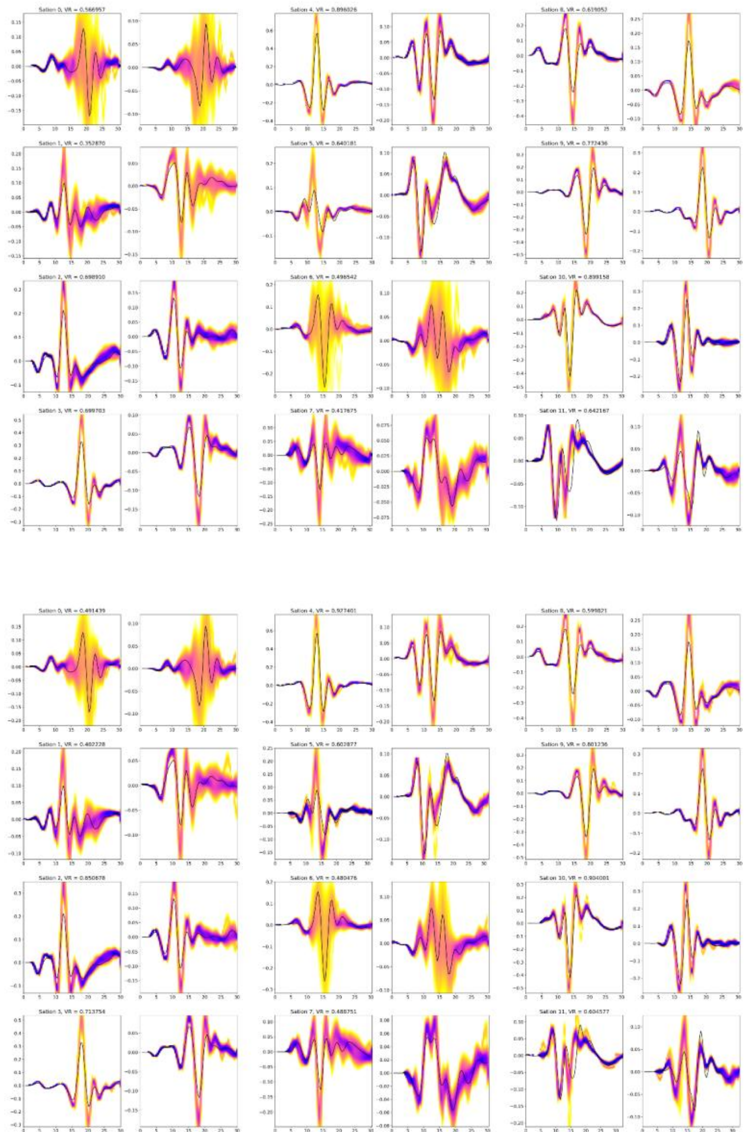

Figure S2: Direct inversion seismogram fit

Data fit of the seismograms by direct inversion method. Station positions are shown in Figure 3a. Black curves: displacement seismograms. Yellow-red heat map: kernel density estimate of the seismograms. Each panel of 6x4 pictures results from a single MCMC run.

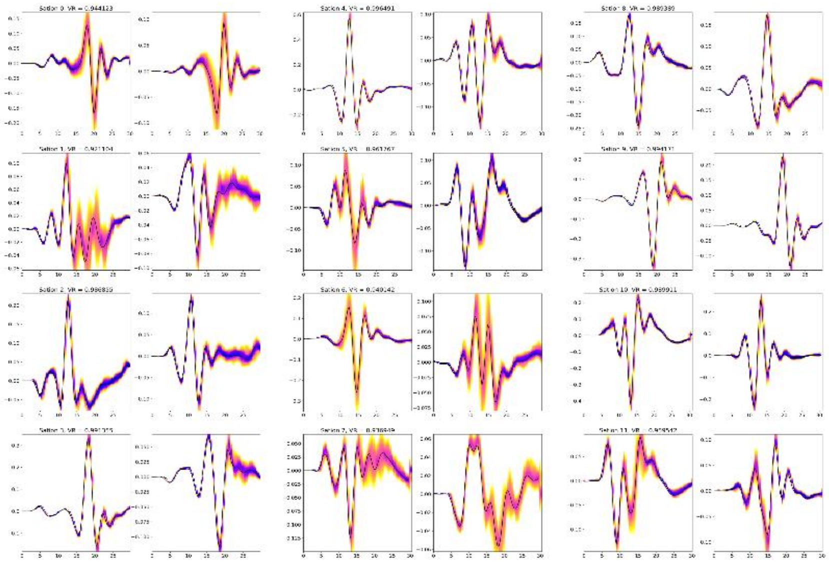

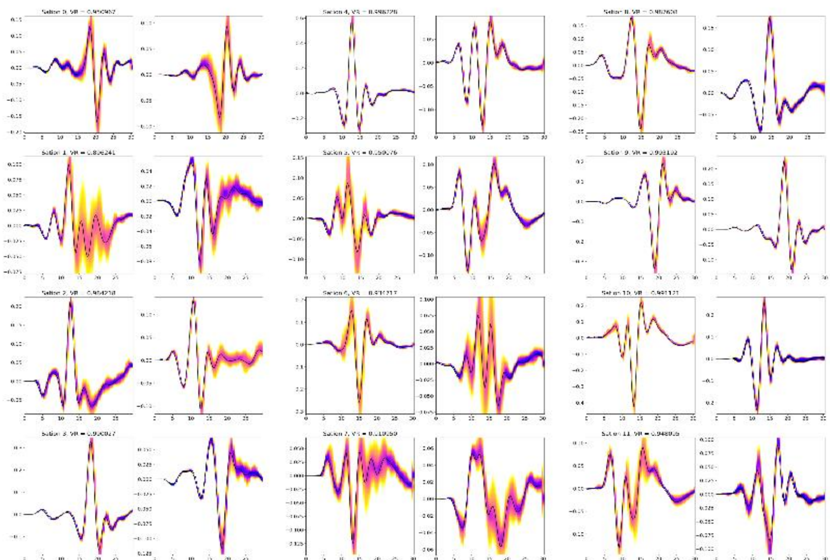

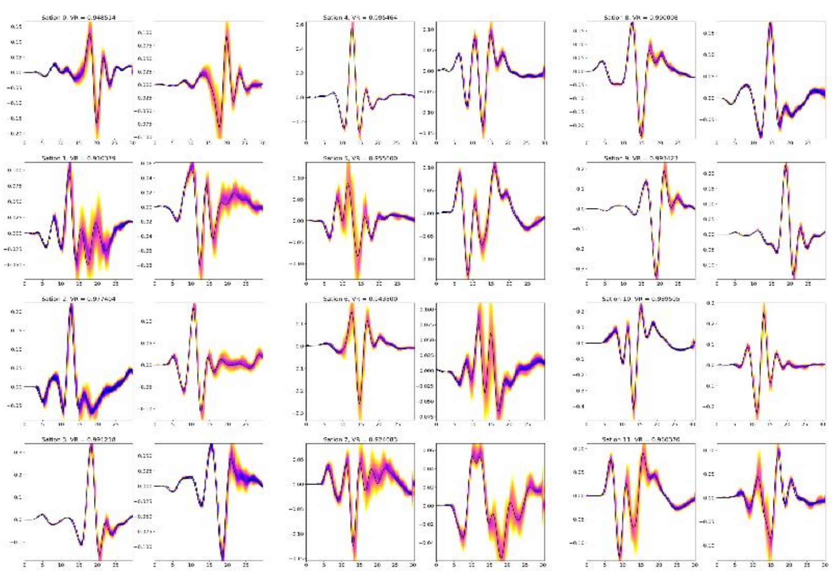

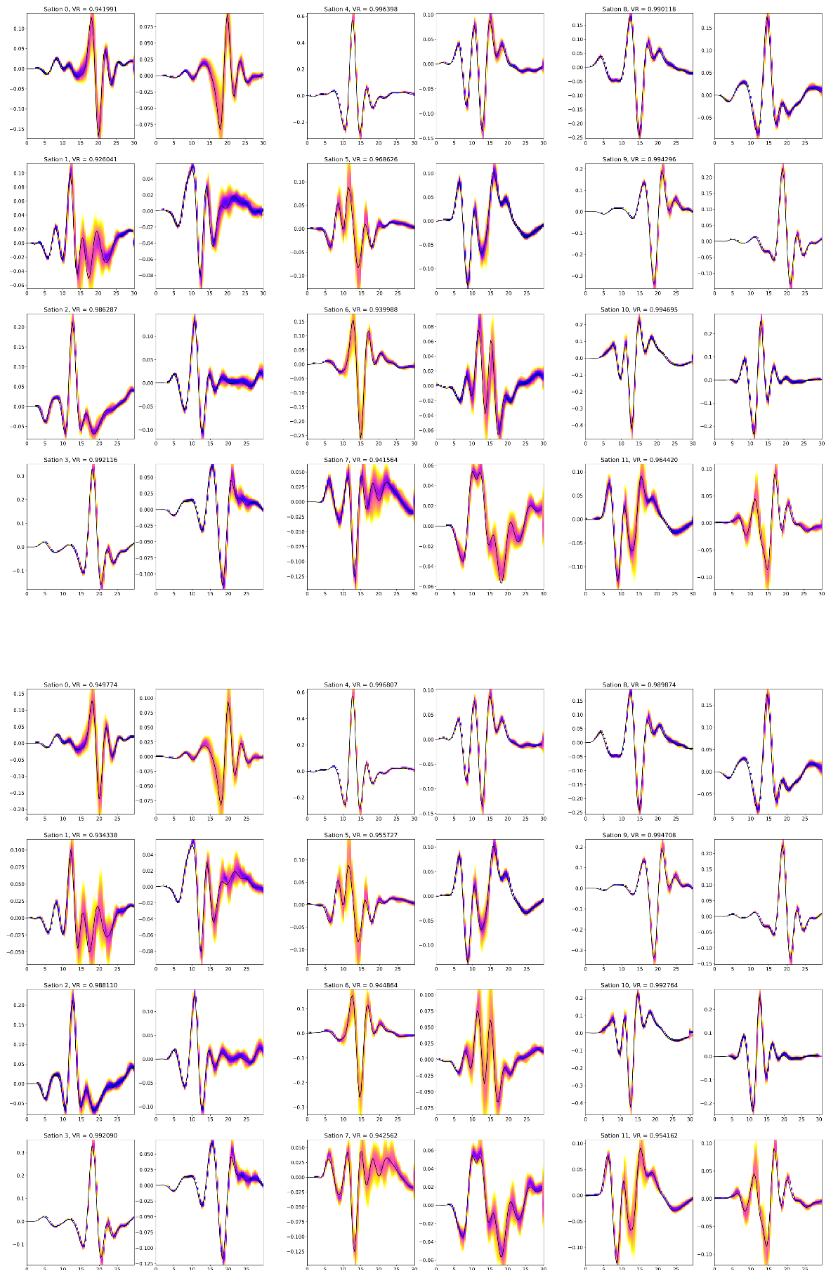

Figure S3: 2-stage inversion seismogram fit

Data fit of the seismograms by the 2-stage inversion method. Station positions are shown in Figure 3a. Black curves: displacement seismograms. Yellow-red heat map: kernel density estimate of the seismograms. Each panel of 6x4 pictures results from a single MCMC run.

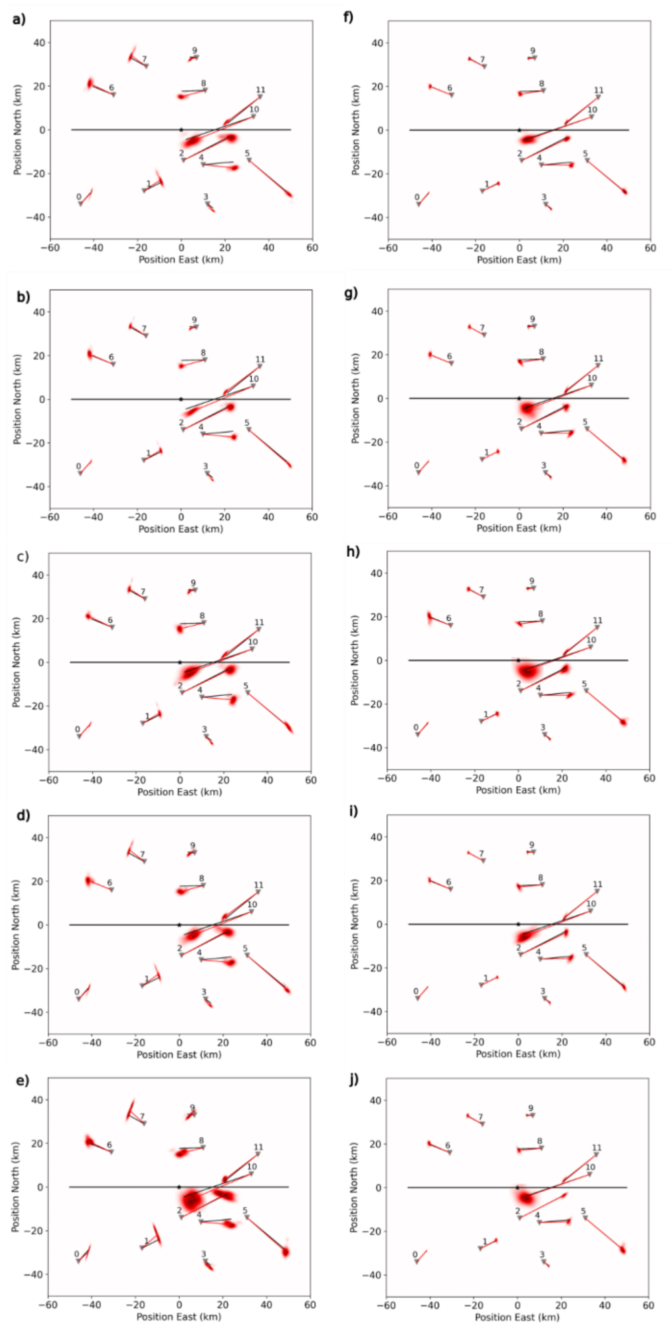

Figure S4: 2-stage inversion seismogram fit

Data fit of the GPS displacements by the direct (a-e) and 2-stage inversion method (f-j). Station positions are shown in Figure 3a. Black arrows: target model displacement. Red arrows: mean inverted displacement. Red heat map: kernel density estimate of inverted displacement.

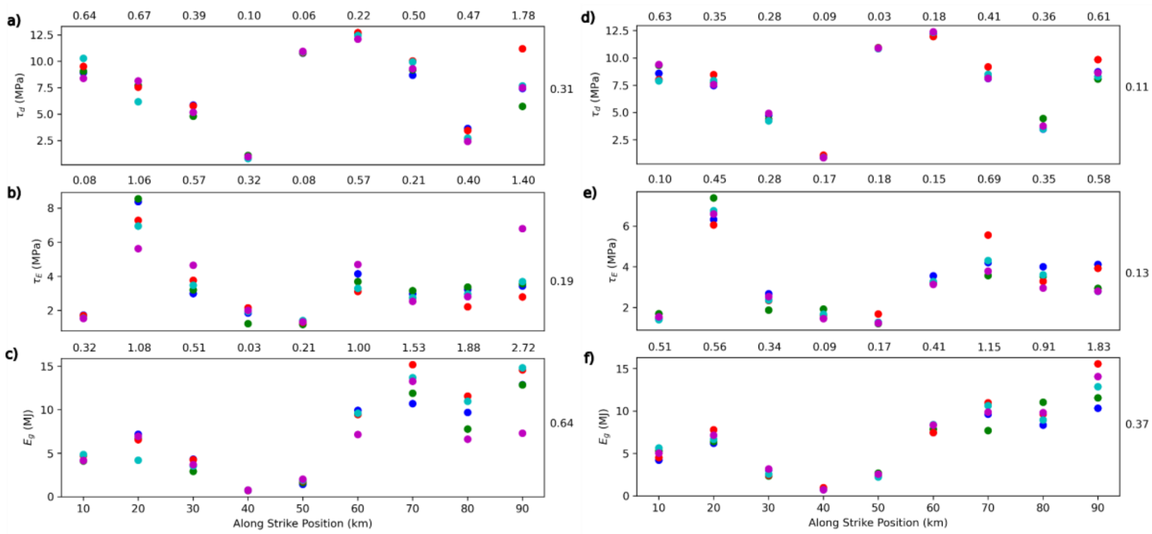

Figure S5

Mean estimates of along-strike distribution of dynamic parameters (stress drop, strength excess and fracture energy) from the 5 runs of the direct dynamic inversion (a-c) and 2-stage dynamic inversion (d-f). The numbers above the plots are values of variance in mean estimates calculated from the 5 different inversions. The numbers on the right are variances of mean estimate averaged over the whole fault.